

Finite-element methods for noncollinear magnetism and spin-orbit coupling in real-space pseudopotential density functional theory

Nikhil Kodali and Phani Motamarri*

Department of Computational and Data Sciences, Indian Institute of Science, Bangalore 560012

We introduce an efficient finite-element approach for large-scale real-space pseudopotential density functional theory (DFT) calculations incorporating noncollinear magnetism and spin-orbit coupling effects. The approach, implemented within the open-source DFT-FE computational framework, fills a significant gap in real-space DFT calculations using finite element basis sets, which offer several advantages over traditional DFT basis sets. In particular, we leverage the local reformulation of DFT electrostatics to derive the finite-element (FE) discretized governing equations involving two-component spinors. To evaluate the widely used GGA exchange-correlation potentials in these governing equations under the locally collinear approximation, we devise a numerical strategy that avoids the computation of ill-defined gradients of magnetization direction near zero magnetization. Additionally, we utilize an efficient self-consistent field iteration approach based on Chebyshev filtered subspace iteration procedure exploiting the sparsity of local and non-local parts of FE discretized Hamiltonian to solve the underlying nonlinear eigenvalue problem based on a two-grid strategy. Furthermore, we propose using a generalized functional within the framework of noncollinear magnetism and spin-orbit coupling with a stationary point at the minima of the Kohn-Sham DFT energy functional to develop a unified framework for computing atomic forces and periodic unit-cell stresses. Validation studies against plane-wave implementations show excellent agreement in ground-state energetics, vertical ionization potentials, magnetic anisotropy energies, band structures, and spin textures. The proposed method achieves up to 8x–11x speedups for semi-periodic and periodic systems with ~ 5000 -7000 electrons in terms of minimum wall times compared to widely used plane-wave implementations on CPUs in addition to exhibiting significant computational advantage on GPUs for material systems with as many as 20,000 electrons. The proposed approach offers a fast, scalable, and systematically convergent framework for large-scale DFT calculations accounting for noncollinear magnetism and spin-orbit coupling, enabling more complex material simulations and extending the range of *ab initio* studies.

I. INTRODUCTION

Spin-orbit coupling (SOC) and noncollinear magnetism are integral for predicting complex material properties in systems with pronounced relativistic effects and magnetic frustration. Spin-orbit coupling is a relativistic effect that gives rise to an interaction that couples an electron's spin and its orbital motion. SOC plays a critical role in stabilizing noncollinear magnetic structures in magnetic materials with heavy elements where the magnetic moments deviate from simple parallel or antiparallel alignments. This interplay is crucial for understanding exotic magnetic behaviors involving spin textures like skyrmions and spin-spirals. Spin-orbit coupling induces exotic electronic behaviors even in non-magnetic materials by lifting degeneracies in the electronic band structure, leading to phenomena such as band splitting and the stabilization of topological phases. The utilization of pseudopotential Density Functional Theory (DFT), a widely adopted first-principles material simulation tool, has been shown to be effective in predicting various material properties when extended to account for spin-orbit coupling [1, 2].

Large-scale DFT calculations accounting for noncollinear magnetism and SOC are essential for accurately

capturing complex physical phenomena, as demonstrated in several recent studies. For instance, Chatratin *et al.* [3] modeled dilute dopants in the semiconductor CdTe using supercells of up to 512 atoms, extrapolating their findings to the dilute limit which may not always be accurate. Similarly, Choi *et al.* [4] employed DFT with 512-atom supercells to investigate skyrmion pinning due to atomic defects in MnSi, noting finite-size effects in their results since the skyrmion size in MnSi (~ 10 nm) exceeds their supercell size (3.4 nm). In another recent work, He and Weng [5] used DFT to study the nonlinear Hall effect in incommensurate Moiré lattices of twisted bilayer WTe_2 , simulating systems of up to 1032 atoms for twist angles as low as 12.3° and could not simulate systems with much lower twist angles. In all these cases, size limitations that can be handled in current DFT implementations, particularly when incorporating SOC and noncollinear magnetism, restricted the ability of these authors to study the desired physics from a first-principles perspective.

Among the various discretization methods employed for computations incorporating noncollinear magnetism and spin-orbit coupling effects in the framework of pseudopotential DFT, the plane-wave (PW) basis is the most widely utilized for solid-state systems, primarily due to its spectral convergence properties, which facilitate computationally efficient calculations. However, these plane-wave based methods suffer from well-known limitations, including poor scalability on parallel computing architectures, which limits their applications to material sys-

* phanim@iisc.ac.in

tems with at most a few thousand electrons. Plane-wave based methods are also inefficient for treating non-periodic systems due to their inability to handle generic boundary conditions. To address these challenges, there has been an increased focus on developing systematically convergent, efficient, and scalable real-space discretization techniques based on finite-difference [6–11], finite-elements [12–26], wavelets [27–29] and other reduced-order basis techniques [30–33]. However, we note that these systematically improvable real-space discretization strategies used in pseudopotential DFT calculations for noncollinear magnetism and spin-orbit coupling are predominantly based on finite-difference methods [34–37]. These strategies have been applied to perform noncollinear DFT calculations on material systems containing up to a maximum of a few thousand electrons.

The finite-element (FE) basis, a relatively new entrant for real-space DFT calculations, is employed in the current work. These basis sets involve compactly supported piecewise polynomials and have emerged as a promising alternative, providing numerous advantages over other commonly used basis sets for density functional theory calculations. In particular, these basis functions can accommodate generic boundary conditions (periodic, semi-periodic, and non-periodic) while providing systematic convergence to the material properties of interest. Most importantly, the locality of these FE basis functions allows the development of computational algorithms that can exploit fine-grained parallelism on modern heterogeneous architectures [38–40], ensuring excellent parallel scalability on distributed systems. Previous studies have shown that FE-based methods can significantly outperform plane-wave methods employing norm-conserving pseudopotential DFT calculations [24, 25] and very recently using the projector augmented method [41] for system sizes greater than 5000 electrons. The open-source DFT-FE code [39] inherits these features and incorporates efficient, scalable solvers for the Kohn-Sham DFT equations involving norm-conserving pseudopotentials within the framework of collinear magnetism. Furthermore, DFT-FE has demonstrated exceptional scalability on massively parallel many-core CPU and hybrid CPU-GPU architectures, handling simulations of material systems with up to 600,000 electrons on up to 200,000 CPU cores and 40,000 GPUs. The finite-element based methods incorporated in DFT-FE have also been used in various scientific studies recently to conduct large-scale DFT calculations involving material systems with tens of thousands of electrons [25, 38, 42–49].

We note that the aforementioned finite-element-based DFT pseudopotential calculations are all limited to the case of collinear magnetism and further do not incorporate spin-orbit effects. This work introduces a local real-space formalism incorporating noncollinear magnetism and spin-orbit coupling (SOC) within the norm-conserving pseudopotential DFT framework amenable for finite-element (FE) discretization building on the DFT-FE computational framework [39, 50]. Further-

more, we propose robust and efficient scalable strategies to evaluate the FE-discretized Hamiltonian and solve the underlying nonlinear generalized eigenvalue problem using a self-consistent field iteration approach. Additionally, we demonstrate that our method can handle fully periodic, non-periodic, and semi-periodic boundary conditions for generic material systems as large as 20,000 electrons within the framework of noncollinear magnetism involving 2-component complex spinors. Moreover, our method offers substantial computational efficiencies over state-of-the-art plane-wave-based approaches for large-scale systems, as demonstrated in this work. Notably, to our knowledge, this work represents the first development of a fast and scalable real-space computational approach incorporating noncollinear magnetism and spin-orbit coupling within the framework of finite-element discretization. We also introduce a generalized force approach to derive atomic forces and stresses within the DFT framework of noncollinear magnetism and SOC.

We adopt the locally collinear approximation to employ the existing approximate exchange-correlation functional forms that are well-tested for spin-collinear cases. The inclusion of spin-orbit interaction in the optimized norm-conserving pseudopotential (ONCV) framework employed in the current work is along the similar lines of Corso and Conte [51]. The key aspects of the current work include: (i) utilizing the local real-space reformulation of the DFT electrostatics [39] to derive the governing equations in terms of the finite-element (FE) discretized Hamiltonian matrix and the 2-component complex spinors to compute the ground-state magnetization and energies, (ii) devising a numerical strategy to evaluate the GGA exchange-correlation potentials in these governing equations, avoiding the computation of ill-defined gradients of magnetization direction near zero magnetization arising within the FE framework using C^0 basis functions, (iii) formulating a unified approach to compute atomic forces and unit-cell stresses by evaluating the directional derivatives of a generalized energy functional proposed in this work, extending the ideas of Methfessel [52], Jacobsen *et al.* [53] to the case of noncollinear magnetism, (iv) developing efficient and scalable methods to build the FE discretized Hamiltonian and thereby compute the action of this Hamiltonian on a trial subspace of vectors efficiently by exploiting the sparsity of local and non-local parts of this Hamiltonian, (v) employing a self-consistent iteration approach based on a Chebyshev filtered subspace iteration procedure that leverages these efficient strategies to solve the underlying nonlinear FE discretized generalized eigenvalue problem. The proposed formulation has been implemented in a distributed environment using both CPUs and GPUs, utilizing the message-passing interface (MPI) for communication across multiple nodes, enabling large-scale DFT calculations that account for noncollinear magnetism and spin-orbit effects. We benchmark the accuracy and performance of our method against plane-wave-based imple-

mentations on various representative non-periodic, semi-periodic, and fully periodic systems. Compared to reference data from plane-wave calculations, our results show excellent agreement in ground-state energies, band structures, vertical ionization potentials, magnetic anisotropy energies, and spin textures. Relative to widely used plane-wave based implementations, our finite-element based approach demonstrates significant computational advantage both in terms of CPU node-hrs and minimum wall time with increasing system sizes.

The remaining sections of the manuscript are organized as follows. Section II briefly introduces the mathematical formulation to account for noncollinear magnetism and spin-orbit coupling using 2-component spinors within norm-conserving pseudopotential DFT formalism and finally discusses the necessary governing equations to be solved utilizing a local reformulation of electrostatics. Subsequently, section III introduces the finite-element discretization for the governing differential equations and details the proposed numerical strategy for evaluating the gradient-corrected exchange-correlation potentials under the locally collinear approximation. Section IV details the efficient and scalable solution procedure for solving the FE discretized generalized eigenvalue problem using a self-consistent field iteration approach and the Chebyshev filtered subspace iteration method. Section V presents comprehensively the accuracy and performance benchmarks of our implementation compared with state-of-the-art plane-wave (PW) codes on representative benchmark systems and large-scale systems. We find that the results obtained from our methodology are well within the bound of chemical accuracy when compared to the state-of-the-art PW codes for a wide range of benchmarks, including total energy, magnetic anisotropy energy, vertical ionization potentials, and band-structures. We also demonstrate up to a 2x reduction in computational cost for systems with $\sim 15,000$ - $20,000$ electrons and $\sim 8x$ - $11x$ speed-ups for semi-periodic and non-periodic systems in terms of minimum wall times compared to widely used plane-wave implementations on CPUs. Furthermore, we also demonstrate the significant computational advantage of our proposed methodology on GPUs. Finally, we conclude with a short discussion summarizing the key findings and outline future prospects arising from this work in section VI

II. MATHEMATICAL FORMULATION

This section will briefly outline the mathematical formulation necessary to account for noncollinear magnetism and spin-orbit coupling within the framework of real-space pseudopotential density functional theory amenable for finite-element discretization in order to compute ground-state energies, forces and periodic unit-cell stresses.

A. Spinor representation of the wavefunctions

Noncollinear magnetism is incorporated in density functional theory by representing the single-electron wavefunctions as 2-component spinors (Ψ_n) [54, 55] given by

$$\Psi_n(\mathbf{r}) = \begin{bmatrix} \psi_n^\uparrow(\mathbf{r}) \\ \psi_n^\downarrow(\mathbf{r}) \end{bmatrix} \quad \forall n = 1, \dots, N_e \quad (1)$$

where N_e denotes the number of electrons in the given material system. The 2×2 Hermitian density matrix ρ in the spin space can then be expressed as

$$\rho(\mathbf{r}) = \begin{bmatrix} \rho^{\uparrow\uparrow}(\mathbf{r}) & \rho^{\uparrow\downarrow}(\mathbf{r}) \\ \rho^{\downarrow\uparrow}(\mathbf{r}) & \rho^{\downarrow\downarrow}(\mathbf{r}) \end{bmatrix} \quad \rho^{\alpha\beta}(\mathbf{r}) = \sum_n f_n \psi_n^{\alpha*} \psi_n^\beta \quad (2)$$

where α and β can be either \uparrow (0) or \downarrow (1) and $*$ denotes the complex conjugate. The above density matrix in the basis of the 2×2 identity matrix (\mathbf{I}) and the Pauli vector ($\vec{\sigma} = \sigma^x \hat{\mathbf{x}} + \sigma^y \hat{\mathbf{y}} + \sigma^z \hat{\mathbf{z}}$) can be written as

$$\rho(\mathbf{r}) = \frac{1}{2} (\rho(\mathbf{r}) \mathbf{I} + \mathbf{m}(\mathbf{r}) \cdot \vec{\sigma}) \quad (3)$$

Here $\rho(\mathbf{r})$, the electron density and $\mathbf{m}(\mathbf{r})$, the magnetization density are given by

$$\rho(\mathbf{r}) = \sum_n f_n \Psi_n^\dagger(\mathbf{r}) \Psi_n(\mathbf{r}) \quad (4)$$

$$\mathbf{m}(\mathbf{r}) = \sum_n f_n \Psi_n^\dagger(\mathbf{r}) \vec{\sigma} \Psi_n(\mathbf{r}) \quad (5)$$

where f_n is the Fermi occupation number corresponding to Ψ_n and \dagger denotes the complex conjugate transpose.

B. Kohn-Sham energy functional and the governing equations

The Kohn-Sham energy functional associated with a material system comprising N_a nuclei and N_e electrons in the norm-conserving pseudopotential framework under the generalized gradient approximation (GGA) is written in terms of the 2-component spinors $\Psi = [\Psi_1, \Psi_2, \dots, \Psi_N]$ with $N \geq N_e$, the vector of atomic coordinates $\mathbf{R} = [\mathbf{R}_1, \mathbf{R}_2, \dots, \mathbf{R}_{N_a}]$, the charge density ρ , and the magnetization density \mathbf{m} , as follows: [54]

$$E[\Psi, \mathbf{R}] = T_s[\Psi] + E_{\text{el}}[\rho, \mathbf{R}] + E_{\text{psp}}[\Psi, \mathbf{R}] + E_{\text{xc}}[\rho, \mathbf{m}, \nabla\rho, \nabla\mathbf{m}] \quad (6)$$

where the kinetic energy of the non-interacting electrons ($T_s[\Psi]$) is given by

$$T_s[\Psi] = \sum_n f_n \int \left(\frac{\nabla \Psi_n^\dagger(\mathbf{r}) \cdot \nabla \Psi_n(\mathbf{r})}{2} \right) d\mathbf{r} \quad (7)$$

while the total electrostatic energy ($E_{\text{el}}[\rho, \mathbf{R}]$) is evaluated by defining the total nuclear charge density

$b(\mathbf{r}, \mathbf{R}) = \sum_a b^a(\mathbf{r} - \mathbf{R}_a)$ with atom-centered smeared nuclear charges for each of the N_a atoms is defined as $b^a(\mathbf{r} - \mathbf{R}_a) \forall a = 1, \dots, N_a$ [39]. To this end, we have

$$E_{\text{el}}[\rho, \mathbf{R}] = \frac{1}{2} \int (\rho(\mathbf{r}) + b(\mathbf{r}, \mathbf{R})) V_{\text{el}}(\mathbf{r}) d\mathbf{r} - \frac{1}{2} \sum_a \int b^a(\mathbf{r}' - \mathbf{R}_a) V_{\text{self}}^a(\mathbf{r}', \mathbf{R}_a) d\mathbf{r}' \quad (8)$$

wherein the total electrostatic potential, $V_{\text{el}}(\mathbf{r}, \mathbf{R})$, and the nuclear self-interaction potential for atom a , $V_{\text{self}}^a(\mathbf{r}, \mathbf{R}_a)$, are obtained as the solutions of the following Poisson equations

$$-\nabla^2 V_{\text{el}}(\mathbf{r}) = 4\pi(\rho(\mathbf{r}) + b(\mathbf{r}, \mathbf{R})) \quad (9)$$

$$-\nabla^2 V_{\text{self}}^a(\mathbf{r}, \mathbf{R}_a) = 4\pi b^a(\mathbf{r} - \mathbf{R}_a) \quad (10)$$

and for the exchange-correlation energy ($E_{\text{xc}}[\rho, \mathbf{m}, \nabla\rho, \nabla\mathbf{m}]$), we use the locally collinear approximation in order to utilize the existing approximate exchange-correlation functionals which have been well tested for the spin-collinear systems and are usually of the form [56]

$$E_{\text{xc}} = \int f_{\text{xc}}(\rho^\uparrow, \rho^\downarrow, \gamma_0, \gamma_1, \gamma_2) d\mathbf{r} \quad (11)$$

where $f_{\text{xc}}(\rho^\uparrow, \rho^\downarrow, \gamma_0, \gamma_1, \gamma_2)$ is the exchange-correlation energy density. To this end, we make the following substitution for the spin-up (ρ^\uparrow) and spin-down (ρ^\downarrow) charge densities.

$$\rho^\uparrow = \frac{\rho + |\mathbf{m}|}{2} \quad \rho^\downarrow = \frac{\rho - |\mathbf{m}|}{2}$$

and the auxiliary quantities typically considered for the gradient-type exchange-correlation functionals are evaluated as

$$\begin{aligned} \gamma_0 &= \frac{\nabla(\rho + |\mathbf{m}|) \cdot \nabla(\rho + |\mathbf{m}|)}{4} \\ \gamma_1 &= \frac{\nabla(\rho + |\mathbf{m}|) \cdot \nabla(\rho - |\mathbf{m}|)}{4} \\ \gamma_2 &= \frac{\nabla(\rho - |\mathbf{m}|) \cdot \nabla(\rho - |\mathbf{m}|)}{4} \end{aligned}$$

We note that the above substitution is not unique, and various other substitutions have been proposed in literature [57–59] to enable the use of collinear-spin exchange-correlation functionals for the noncollinear spin case.

For the pseudopotential approximation we utilize the Optimized Norm-Conserving Vanderbilt (ONCV) [60] pseudopotentials which allow for the following separable form for the pseudopotential contribution to the energy functional, $E_{\text{psp}}[\Psi] = E_{\text{loc}}[\Psi] + E_{\text{nloc}}[\Psi]$. The local pseudopotential energy contribution, $E_{\text{loc}}[\Psi]$, can be evaluated as

$$E_{\text{loc}}[\Psi, \mathbf{R}] = \int (V_{\text{loc}}(\mathbf{r}) - V_{\text{self}}(\mathbf{r})) \rho(\mathbf{r}) d\mathbf{r} \quad (12)$$

where the local pseudopotential operator can be written as the sum of the atom-dependent local pseudopotentials, $V_{\text{loc}}(\mathbf{r}) = \sum_a V_{\text{loc}}^a(\mathbf{r} - \mathbf{R}_a)$ and the nuclear self-interaction potential is given by $V_{\text{self}}(\mathbf{r}) = \sum_a V_{\text{self}}^a(\mathbf{r}, \mathbf{R}_a)$. Note that V_{self} is subtracted here to account for the inclusion of the nuclear potential arising due to smeared charges [24, 39] in the electrostatic energy term in eq. (8)

For the case of spin-orbit coupling in the ONCV framework [51], the non-local pseudopotential contribution to the energy functional, $E_{\text{nloc}}[\Psi]$, can be expressed as

$$E_{\text{nloc}}[\Psi] = \sum_n f_n \int \int \Psi_n^\dagger(\mathbf{r}) \mathbf{V}_{\text{nloc}}(\mathbf{r}, \mathbf{r}') \Psi_n(\mathbf{r}') d\mathbf{r} d\mathbf{r}' \quad (13)$$

and the non-local pseudopotential operator, $\mathbf{V}_{\text{nloc}}(\mathbf{r}, \mathbf{r}')$ is given by

$$\mathbf{V}_{\text{nloc}}(\mathbf{r}, \mathbf{r}') = \sum_a \sum_{\chi\chi'} \mathbf{D}^{\gamma_a, \chi, \chi'} p_\chi^a(\mathbf{r} - \mathbf{R}_a) p_{\chi'}^a(\mathbf{r}' - \mathbf{R}_a) \quad (14)$$

where γ_a denotes the atom type of atom a and we define composite indices $\chi = \{\tau, l, j, m\}$ and $\chi' = \{\tau', l', j', m'\}$ such that l (l') and j (j') denote the orbital and the total angular momentum respectively, m (m') denotes the projection of the angular momentum on the quantization axis. Further, $p_\chi^a(\mathbf{r})$ is the non-local projector function indexed by τ centered at atom a , and the angular momentum components l, j and m , while $\mathbf{D}^{\gamma_a, \chi, \chi'}$ are the 2×2 matrices representing the non-local pseudopotential coefficients.

The Euler-Lagrange equations corresponding to minimizing the energy functional in eq. (6) subject to the orthogonality constraint $\int \Psi_n^\dagger(\mathbf{r}) \Psi_{n'}(\mathbf{r}) d\mathbf{r} = \delta_{nn'}$ can be written as the following nonlinear Hermitian eigenvalue problem

$$\mathcal{H}\Psi_n = \epsilon_n \Psi_n \quad (15)$$

to be solved for eigenfunctions corresponding to N smallest eigenvalues, where $\{\epsilon_n\}$ are the eigenvalues and $\{\Psi_n\}$ are the corresponding eigenfunctions of the Hamiltonian operator \mathcal{H} which are the canonical wavefunctions that minimize the energy functional eq. (6). We note that \mathcal{H} can be decomposed as $\mathcal{H} = \mathcal{H}^{\text{loc}} + \mathcal{H}^{\text{nloc}}$ with \mathcal{H}^{loc} defined by

$$\mathcal{H}^{\text{loc}} = \left[-\frac{1}{2} \nabla^2 + V_{\text{eff}}(\mathbf{r}) \right] \mathbf{I} + \mathbf{B}_{\text{xc}} \cdot \vec{\sigma} \quad (16)$$

where \mathbf{I} is the 2×2 identity matrix and $\vec{\sigma}$ is the Pauli vector. The effective potential and the XC fields are defined as

$$V_{\text{eff}}(\mathbf{r}) = V_{\text{el}}(\mathbf{r}) + V_{\text{xc}}(\mathbf{r}) + (V_{\text{loc}}(\mathbf{r}) - V_{\text{self}}(\mathbf{r})) \quad (17)$$

$$V_{\text{xc}}(\mathbf{r}) = \frac{\delta E_{\text{xc}}}{\delta \rho(\mathbf{r})} \quad \mathbf{B}_{\text{xc}} = \frac{\delta E_{\text{xc}}}{\delta \mathbf{m}(\mathbf{r})} \quad (18)$$

and $\mathcal{H}^{\text{nlloc}}$ is defined as follows

$$\mathcal{H}^{\text{nlloc}}\Psi_n := \int \mathbf{V}_{\text{nlloc}}(\mathbf{r}, \mathbf{r}')\Psi_n(\mathbf{r}')d\mathbf{r}' \quad (19)$$

Using the separable form of the non-local pseudopotential operator from eq. (14), we have

$$\int \mathbf{V}_{\text{nlloc}}(\mathbf{r}, \mathbf{r}')\Psi_n(\mathbf{r}')d\mathbf{r}' = \sum_a \sum_{\chi\chi'} p_{\chi}^a(\mathbf{r} - \mathbf{R}_a) \mathbf{D}^{\gamma_a, \chi, \chi'} \int p_{\chi'}^a(\mathbf{r}' - \mathbf{R}_a) \Psi_n(\mathbf{r}')d\mathbf{r}' \quad (20)$$

All the integrals in eqs. (7) to (8) and (11) to (13) are over the entire space (\mathbb{R}^3) for the case of non-periodic systems. For the case of periodic systems, the energy functional in eq. (6) represents the energy per the periodic unit cell and all the integrals involving \mathbf{r} in eqs. (7) to (8) and (11) to (13) are over this unit-cell and those involving \mathbf{r}' are over the entire space \mathbb{R}^3 . Furthermore, we can now invoke the Bloch theorem, $\Psi_n(\mathbf{r}) = e^{i\mathbf{k}\cdot\mathbf{r}}\mathbf{u}_{n\mathbf{k}}(\mathbf{r})$ with $\mathbf{u}_{n\mathbf{k}}(\mathbf{r})$ denoting the 2-component complex-valued periodic Bloch wavefunctions and consequently, the summations over the eigenvector index accounting for the Brillouin zone integration can be written as

$$\sum_n f_n \rightarrow \sum_n \int_{BZ} f_{n\mathbf{k}} d\mathbf{k} \quad (21)$$

where \int_{BZ} denotes the volume average of the integral over the Brillouin zone corresponding to the periodic

unit-cell Ω_p and $f_{n\mathbf{k}}$ are the orbital occupation numbers corresponding to $\mathbf{u}_{n\mathbf{k}}$. To this end, the nonlinear eigenvalue problem in eq. (15) can be recast as follows:

$$\mathcal{H}^{\mathbf{k}}\mathbf{u}_{n\mathbf{k}} = \epsilon_{n\mathbf{k}}\mathbf{u}_{n\mathbf{k}} \quad (22)$$

where the transformed \mathbf{k} -dependent Hamiltonian operator is defined as $\mathcal{H}^{\mathbf{k}} = e^{-i\mathbf{k}\cdot\mathbf{r}}\mathcal{H}e^{i\mathbf{k}\cdot\mathbf{r}} = \mathcal{H}^{\mathbf{k},\text{loc}} + \mathcal{H}^{\mathbf{k},\text{nlloc}}$. Here, $\mathcal{H}^{\mathbf{k},\text{loc}}$ is given by

$$\mathcal{H}^{\mathbf{k},\text{loc}} = \left[-\frac{1}{2}\nabla^2 - i\mathbf{k}\cdot\nabla + \frac{|\mathbf{k}|^2}{2} + V_{\text{eff}}(\mathbf{r}) \right] \mathbf{I} + \frac{\delta E_{\text{xc}}}{\delta \mathbf{m}(\mathbf{r})} \cdot \boldsymbol{\sigma} \quad (23)$$

and $\mathcal{H}^{\mathbf{k},\text{nlloc}}$ is given by

$$\mathcal{H}^{\mathbf{k},\text{nlloc}}\mathbf{u}_{n\mathbf{k}} = \sum_{a \in \Omega_p} \sum_{\chi\chi'} \sum_q e^{-i\mathbf{k}\cdot(\mathbf{r}-\mathbf{L}_q)} p_{\chi}^a(\mathbf{r} - \mathbf{L}_q - \mathbf{R}_a) \mathbf{D}^{\gamma_a, \chi, \chi'} \int_{\Omega_p} \sum_{q'} e^{i\mathbf{k}\cdot(\mathbf{r}'-\mathbf{L}_{q'})} p_{\chi'}^a(\mathbf{r}' - \mathbf{L}_{q'} - \mathbf{R}_a) \mathbf{u}_{n\mathbf{k}}(\mathbf{r}')d\mathbf{r}' \quad (24)$$

where \mathbf{L}_q and $\mathbf{L}_{q'}$ are the lattice vectors.

To summarize, the governing equations to be solved for density functional theory incorporating noncollinear magnetism and spin-orbit coupling are given by

$$\begin{aligned} \mathcal{H}^{\mathbf{k}}\mathbf{u}_{n\mathbf{k}} &= \epsilon_{n\mathbf{k}}\mathbf{u}_{n\mathbf{k}} \\ \mathcal{H}^{\mathbf{k}} &= \mathcal{H}^{\mathbf{k},\text{loc}} + \mathcal{H}^{\mathbf{k},\text{nlloc}} \\ \mathcal{H}^{\mathbf{k},\text{loc}} &= \left[-\frac{1}{2}\nabla^2 - i\mathbf{k}\cdot\nabla + \frac{|\mathbf{k}|^2}{2} + V_{\text{eff}}(\mathbf{r}) \right] \mathbf{I} + \mathbf{B}_{\text{xc}} \cdot \boldsymbol{\sigma} \\ \mathcal{H}^{\mathbf{k},\text{nlloc}}\mathbf{u}_{n\mathbf{k}} &= \sum_{a \in \Omega_p} \sum_{\chi\chi'} \sum_q e^{-i\mathbf{k}\cdot(\mathbf{r}-\mathbf{L}_q)} p_{\chi}^a(\mathbf{r} - \mathbf{L}_q - \mathbf{R}_a) \mathbf{D}^{\gamma_a, \chi, \chi'} \int_{\Omega_p} \sum_{q'} e^{i\mathbf{k}\cdot(\mathbf{r}'-\mathbf{L}_{q'})} p_{\chi'}^a(\mathbf{r}' - \mathbf{L}_{q'} - \mathbf{R}_a) \mathbf{u}_{n\mathbf{k}}(\mathbf{r}')d\mathbf{r}' \\ V_{\text{eff}}(\mathbf{r}) &= V_{\text{el}}(\mathbf{r}) + V_{\text{xc}}(\mathbf{r}) + (V_{\text{loc}}(\mathbf{r}) - V_{\text{self}}(\mathbf{r})) \\ V_{\text{loc}}(\mathbf{r}) &= \sum_q \sum_{a \in \Omega_p} V_{\text{loc}}^a(\mathbf{r} - \mathbf{L}_q - \mathbf{R}_a) \quad V_{\text{self}}(\mathbf{r}) = \sum_q \sum_{a \in \Omega_p} V_{\text{self}}^a(\mathbf{r}, \mathbf{L}_q + \mathbf{R}_a) \\ V_{\text{xc}}(\mathbf{r}) &= \frac{\delta E_{\text{xc}}}{\delta \rho(\mathbf{r})} \quad \mathbf{B}_{\text{xc}} = \frac{\delta E_{\text{xc}}}{\delta \mathbf{m}(\mathbf{r})} \\ -\nabla^2 V_{\text{el}}(\mathbf{r}) &= 4\pi(\rho(\mathbf{r}) + b(\mathbf{r}, \mathbf{R})) \\ -\nabla^2 V_{\text{self}}^a(|\mathbf{r} - \mathbf{R}_a|) &= 4\pi b^a(|\mathbf{r} - \mathbf{R}_a|) \end{aligned} \quad (25)$$

This nonlinear eigenvalue problem can be formulated as a fixed point iteration problem as

$$F[(\rho, \mathbf{m})] = (\rho, \mathbf{m}) \quad (26)$$

where the map $F[(\rho_{in}, \mathbf{m}_{in})] = (\rho_{out}, \mathbf{m}_{out})$ represents the computation of V_{eff}^{in} and $\mathbf{B}_{\text{xc}}^{in}$ using a guess of input densities $(\rho_{in}, \mathbf{m}_{in})$, solving eigenvalue problem given by eq. (25) and computing $(\rho_{out}, \mathbf{m}_{out})$ using eqs. (4)

and (5).

Upon obtaining the solution of the above fixed-point iteration to a required tolerance on $\|\rho_{out} - \rho_{in}\|$ and $\|\mathbf{m}_{out} - \mathbf{m}_{in}\|$, the total free energy (per unit-cell in case of a periodic system) can be obtained through the double-counting method [61] as

$$E_0 = \sum_n \int_{BZ} f_{n\mathbf{k}} \epsilon_{n\mathbf{k}} d\mathbf{k} - \int (V_{\text{elxc}}^{in} \rho_{out} + \mathbf{B}_{\text{xc}}^{in} \cdot \mathbf{m}_{out}) d\mathbf{r} + E_{\text{el}}[\rho_{out}] + E_{\text{xc}}[\rho_{out}, \mathbf{m}_{out}] + E_{\text{ent}}[f_{n\mathbf{k}}] \quad (27)$$

Where $V_{\text{elxc}} = V_{\text{el}} + V_{\text{xc}}$ and the entropic energy contribution ($-TS$ where T is the temperature and S is the entropy), E_{ent} , is given by

$$E_{\text{ent}} = k_B T \sum_n \int_{BZ} f_{n\mathbf{k}} \ln(f_{n\mathbf{k}}) d\mathbf{k} + k_B T \sum_n \int_{BZ} (1 - f_{n\mathbf{k}}) \ln(1 - f_{n\mathbf{k}}) d\mathbf{k} \quad (28)$$

We will now discuss the evaluation of the derivatives of energy, specifically the atomic forces and unit-cell stresses.

C. Derivatives of energy: Atomic forces and cell-stresses

In order to compute the derivative of energy, we make use of the configurational force approach previously used by Das *et al.* [39], Motamarri and Gavini [50], Rufus and Gavini [62] in order to compute the derivatives for the spin-collinear and spin unpolarized cases. To this end, the starting point of these works to evaluate the configurational force is to consider the Kohn-Sham energy functional with the non-orthogonal electronic wavefunctions and the single-particle density matrix as independent fields. This makes the derivation of configurational forces non-trivial and makes it even more challenging to account for two-component spinors and the 2×2 density matrix arising in noncollinear magnetism. Consequently, in this work, we introduce a generalized energy functional in the spirit of energy expression given in eq. (27) as the

starting point of our derivation, extending the ideas of Methfessel [52], Jacobsen *et al.* [53] to the case of non-collinear magnetism. This energy functional is given by

$$\begin{aligned} \tilde{E}[\tilde{V}, \tilde{\mathbf{B}}, \tilde{\rho}, \tilde{\mathbf{m}}, \tilde{f}_{n\mathbf{k}}] &= \sum_n \int_{BZ} \tilde{f}_{n\mathbf{k}} \epsilon_{n\mathbf{k}}[\tilde{V}, \tilde{\mathbf{B}}] d\mathbf{k} \\ &- \int (\tilde{V} \tilde{\rho} + \tilde{\mathbf{B}} \cdot \tilde{\mathbf{m}}) d\mathbf{r} + E_{\text{el}}[\tilde{\rho}] + E_{\text{xc}}[\tilde{\rho}, \tilde{\mathbf{m}}] \\ &+ E_{\text{ent}}[\tilde{f}_{n\mathbf{k}}] + \mu \left(N_e - \sum_n \int_{BZ} \tilde{f}_{n\mathbf{k}} d\mathbf{k} \right) \end{aligned} \quad (29)$$

and has the constraint on the number of electrons imposed -via- the Lagrange multiplier μ . In the above functional 29, we treat the potential \tilde{V} , the magnetic field $\tilde{\mathbf{B}}$, the total charge density $\tilde{\rho}$, the magnetization density vector $\tilde{\mathbf{m}}$ and the occupation numbers $\tilde{f}_{n\mathbf{k}}$ as the variational parameters. Note that here, $\epsilon_{n\mathbf{k}}[\tilde{V}, \tilde{\mathbf{B}}]$ are defined as the eigenvalues corresponding to the eigenvalue problem defined by

$$\begin{aligned} \mathcal{H}^{\mathbf{k}} \mathbf{u}_{n\mathbf{k}} &= \epsilon_{n\mathbf{k}} \mathbf{u}_{n\mathbf{k}} \\ \mathcal{H}^{\mathbf{k}} &= \mathcal{H}^{\mathbf{k}, \text{loc}} + \mathcal{H}^{\mathbf{k}, \text{nloc}} \\ \mathcal{H}^{\mathbf{k}, \text{loc}} &= \left[-\frac{1}{2} \nabla^2 - i\mathbf{k} \cdot \nabla + \frac{|\mathbf{k}|^2}{2} + V_{\text{eff}}(\mathbf{r}) \right] \mathbf{I} + \tilde{\mathbf{B}} \cdot \boldsymbol{\sigma} \\ V_{\text{eff}}(\mathbf{r}) &= \tilde{V} + (V_{\text{loc}}(\mathbf{r}) - V_{\text{self}}(\mathbf{r})) \end{aligned} \quad (30)$$

with $\mathcal{H}^{\mathbf{k}, \text{nloc}}$ defined by eq. (24) This functional in eq. (29) has a stationary point at the minima corresponding to Kohn-Sham DFT energy functional (see appendix A for the proof). Let $\tilde{E}_S = \tilde{E}[\tilde{V} = V_{\text{elxc}}, \tilde{\mathbf{B}} = \mathbf{B}_{\text{xc}}, \tilde{\rho} = \rho, \tilde{\mathbf{m}} = \mathbf{m}, \tilde{f}_{n\mathbf{k}} = f_{n\mathbf{k}}] = E_0$ denote the stationary point of this functional.

We now consider a parametrized perturbation of the underlying space described by $\boldsymbol{\tau}^\varepsilon$ which maps a point \mathbf{r} in the unperturbed space to a point $\mathbf{r}^\varepsilon = \boldsymbol{\tau}^\varepsilon(\mathbf{r})$ in the perturbed space. We also define the generator of this perturbation as $\boldsymbol{\Upsilon} = \left. \frac{d\boldsymbol{\tau}^\varepsilon}{d\varepsilon} \right|_{\varepsilon=0}$, in this framework and we can compute the configurational force due to the perturbation $\boldsymbol{\tau}^\varepsilon$ by evaluating the following directional derivative (see appendix B for the derivation of the generalized force expression).

$$\left. \frac{d\tilde{E}_S(\boldsymbol{\tau}^\varepsilon)}{d\varepsilon} \right|_{\varepsilon=0} = \left. \frac{d\tilde{E}_S^\varepsilon}{d\varepsilon} \right|_{\varepsilon=0} = \int_{\Omega_p} \mathbf{E} : \nabla \boldsymbol{\Upsilon} d\mathbf{r} + \sum_{a \in \Omega_p} \int_{\mathbb{R}^3} \mathbf{E}^a : \nabla \boldsymbol{\Upsilon} d\mathbf{r} + F^{\text{psp, nloc}} + F^K + F^{\text{ext, corr}} + F^{\text{sm}} \quad (31)$$

where ‘:’ denotes a tensor contraction and the rank-2 tensor \mathbf{E}^a is given by

$$\mathbf{E}^a = \frac{1}{8\pi} (\nabla V_{\text{self}}^a \cdot \nabla V_{\text{self}}^a) \mathbf{I} - \frac{1}{4\pi} \nabla V_{\text{self}}^a \otimes \nabla V_{\text{self}}^a \quad (32)$$

where ‘ \otimes ’ and ‘ \cdot ’ denote the outer and inner products over the spatial dimensions respectively.

Similarly the rank-2 tensor \mathbf{E} is given by

$$\begin{aligned} \mathbf{E} = & \left(\sum_n \int_{BZ} \frac{f_{nk}}{2} \left(\nabla \mathbf{u}_{nk}^\dagger \cdot \nabla \mathbf{u}_{nk} + (|\mathbf{k}|^2 - \epsilon_{nk}) \mathbf{u}_{nk}^\dagger \mathbf{u}_{nk} - i \mathbf{u}_{nk}^\dagger \mathbf{k} \cdot \nabla \mathbf{u}_{nk} \right) d\mathbf{k} + (V_{\text{loc}} - V_{\text{self}}) \rho + f_{\text{xc}} + \rho V_{\text{el}} - \frac{|\nabla V_{\text{el}}|^2}{8\pi} \right) \mathbf{I} \\ & - \sum_n \int_{BZ} \frac{f_{nk}}{2} \left(\nabla \mathbf{u}_{nk}^\dagger \otimes \nabla \mathbf{u}_{nk} + \nabla \mathbf{u}_{nk} \otimes \nabla \mathbf{u}_{nk}^\dagger - i \mathbf{u}_{nk}^\dagger \nabla \mathbf{u}_{nk} \otimes \mathbf{k} \right) d\mathbf{k} + \frac{1}{4\pi} \nabla V_{\text{el}} \otimes \nabla V_{\text{el}} \\ & - \frac{\partial f_{\text{xc}}}{\partial \nabla \rho} \otimes \nabla \rho - \frac{\partial f_{\text{xc}}}{\partial \nabla |\mathbf{m}|} \otimes \nabla |\mathbf{m}| \quad (33) \end{aligned}$$

The term $F^{\text{psp,nloc}}$ is given by $F^{\text{psp,nloc}} = F_{\text{nloc}}^\dagger + F_{\text{nloc}}$ where F_{nloc} is given by

$$\begin{aligned} F_{\text{nloc}} = & \sum_{a \in \Omega_p} \sum_{\chi \chi'} \sum_q \sum_n \int_{BZ} \left[\int_{\Omega_p} \left(\mathbf{u}_{nk}^\dagger(\mathbf{r}) e^{-i\mathbf{k} \cdot (\mathbf{r} - \mathbf{L}_q)} p_\chi^a(\mathbf{r} - \mathbf{L}_q - \mathbf{R}_a) \right) d\mathbf{r} \mathbf{D}^{\gamma_a, \chi, \chi'} \int_{\Omega_p} \left(\sum_{q'} e^{i\mathbf{k} \cdot (\mathbf{r}' - \mathbf{L}_{q'})} \right. \right. \\ & \left. \left. p_{\chi'}^a(\mathbf{r}' - \mathbf{L}_{q'} - \mathbf{R}_a) \left(-(\boldsymbol{\Upsilon}(\mathbf{r}') - \boldsymbol{\Upsilon}(\mathbf{R}_a + \mathbf{L}_{q'})) \cdot \nabla \mathbf{u}_{nk}(\mathbf{r}') - i\mathbf{k} \cdot \boldsymbol{\Upsilon}(\mathbf{R}_a) \mathbf{u}_{nk}(\mathbf{r}') \right) \right) d\mathbf{r}' \right] d\mathbf{k} \quad (34) \end{aligned}$$

The term F^K is given by

$$\begin{aligned} F^K = & \sum_n \int_{BZ} \int_{\Omega_p} \left[-i \mathbf{u}_{nk}^\dagger \frac{\partial \mathbf{k}^\varepsilon}{\partial \varepsilon} \Big|_{\varepsilon=0} \cdot \nabla \mathbf{u}_{nk} + \frac{1}{2} \frac{\partial}{\partial \varepsilon} \{ |\mathbf{k}^\varepsilon|^2 \} \Big|_{\varepsilon=0} \mathbf{u}_{nk}^\dagger \mathbf{u}_{nk} \right] d\mathbf{r} d\mathbf{k} \\ & + \sum_{a \in \Omega_p} \sum_{\chi \chi'} \sum_q \sum_n \frac{\partial}{\partial \varepsilon} \left\{ \int_{BZ} \left[\int_{\Omega_p} \left(\mathbf{u}_{nk}^\dagger(\mathbf{r}) e^{-i\mathbf{k}^\varepsilon \cdot (\mathbf{r} - \mathbf{L}_q)} p_\chi^a(\mathbf{r} - \mathbf{L}_q - \mathbf{R}_a) \right) d\mathbf{r} \right. \right. \\ & \left. \left. \mathbf{D}^{\gamma_a, \chi, \chi'} \int_{\Omega_p} \left(\sum_{q'} e^{i\mathbf{k}^\varepsilon \cdot (\mathbf{r}' - \mathbf{L}_{q'})} p_{\chi'}^a(\mathbf{r}' - \mathbf{L}_{q'} - \mathbf{R}_a) \mathbf{u}_{nk}(\mathbf{r}') \right) d\mathbf{r}' \right] d\mathbf{k} \right\} \Big|_{\varepsilon=0} \quad (35) \end{aligned}$$

The term $F^{\text{ext,corr}}$ is given by

$$\begin{aligned} F^{\text{ext,corr}} = & \sum_{a \in \Omega_p} \sum_q \int_{\Omega_p} \rho \left(\nabla V_{\text{loc}}^a(\mathbf{r} - \mathbf{R}_a - \mathbf{L}_q) \cdot (\boldsymbol{\Upsilon}(\mathbf{r}) - \boldsymbol{\Upsilon}(\mathbf{R}_a + \mathbf{L}_q)) - \nabla V_{\text{self}}^a(\mathbf{r}, \mathbf{R}_a + \mathbf{L}_q) \cdot \boldsymbol{\Upsilon}(\mathbf{r}) \right. \\ & \left. - \frac{\partial V_{\text{self}}^a(\mathbf{r}, b^a(\mathbf{r}^\varepsilon - \mathbf{R}_a^\varepsilon - \mathbf{L}_q^\varepsilon))}{\partial \varepsilon} \Big|_{\varepsilon=0} \right) d\mathbf{r} \quad (36) \end{aligned}$$

Finally, the term F^{sm} is given by

$$F^{\text{sm}} = \sum_{a \in \Omega_p} \sum_q \int_{\Omega_p} b^a(\mathbf{r} - \mathbf{R}_a - \mathbf{L}_q) \nabla V_{\text{el}} \cdot (\boldsymbol{\Upsilon}(\mathbf{r}) - \boldsymbol{\Upsilon}(\mathbf{R}_a + \mathbf{L}_q)) d\mathbf{r} - \sum_{a \in \Omega_p} \int_{\mathbb{R}^3} b^a(\mathbf{r} - \mathbf{R}_a) \nabla V_{\text{self}}^a \cdot (\boldsymbol{\Upsilon}(\mathbf{r}) - \boldsymbol{\Upsilon}(\mathbf{R}_a)) d\mathbf{r} \quad (37)$$

Now, the atomic forces and cell stress can be computed by choosing appropriate generators ($\boldsymbol{\Upsilon}$). The i^{th} component of the force on atom j can be computed using a generator whose i^{th} component is compactly supported around atom j , the other components of the generator being zero. Cell stresses can be evaluated using a generator corresponding to an appropriate affine transformation. We refer to earlier works [39, 50, 62] for further discussion on the choice of the generator and efficient

evaluation of the terms arising in eq. (31).

III. FINITE-ELEMENT BASED COMPUTATIONAL METHODOLOGY

In this section, we will discuss the higher-order finite-element based numerical methodologies for solving the Kohn-Sham eigenvalue problems in eqs. (15) and (22).

To this end, we first provide a brief overview of the finite-element (FE) basis and describe the discretization of the underlying DFT governing equations involving noncollinear magnetism with spin-orbit coupling effects. Subsequently, we describe the computation of the effective potential terms in the discrete FE setting, followed by the numerical methodology to solve the resulting discretized nonlinear generalized eigenvalue problem. Furthermore, we provide a brief discussion of the efficient numerical implementation strategies underlying the proposed methodology that is well-suited for modern super-computing architectures.

A. Finite-element discretization

In the finite-element (FE) method, the given spatial domain of interest is decomposed into non-overlapping subdomains called finite-elements (cells) by generating an FE mesh. The key aspect of this finite-element subspace is that the underlying basis functions are systematically convergent, compactly supported, piecewise C^0 continuous polynomials [63–66], amenable for massive parallelization. The advantages provided by higher-order adaptive spectral finite-element based methods to solve the Kohn-Sham DFT problem have been discussed in prior works [18, 22, 24, 39] in the context of norm-conserving pseudopotentials and all-electron DFT calculations within the framework of collinear magnetism.

Within the framework of noncollinear magnetism, the finite-element discretization of the 2-component complex spinors is given by

$$\begin{aligned} \mathbf{u}_{n\mathbf{k}}^{h,p}(\mathbf{r}) &= \sum_{I=0}^{M^{h,p}-1} \begin{bmatrix} u_{n\mathbf{k}}^{I,\uparrow} \\ u_{n\mathbf{k}}^{I,\downarrow} \end{bmatrix} N_I^{h,p}(\mathbf{r}) \\ &= \sum_{I=0}^{M^{h,p}-1} \mathbf{u}_{n\mathbf{k}}^I N_I^{h,p}(\mathbf{r}) \end{aligned} \quad (38)$$

where $\mathbf{u}_{n\mathbf{k}}^I$ are the 2-component linear combination coefficients associated with the discretized complex Bloch wavefunction $\mathbf{u}_{n\mathbf{k}}^{h,p}(\mathbf{r})$ and $N_I^{h,p}(\mathbf{r}) : 0 \leq I < M^{h,p}$ are the 3D tensor-structured FE polynomial basis constructed from 1D Lagrange polynomials of degree p defined over Gauss Lobatto Legendre (GLL) nodal points [63], generated using the nodes of the FE triangulation \mathcal{T}^h with the characteristic mesh size denoted by h . Consequently, the FE discretization of the nonlinear eigenvalue problem corresponding to eq. (22) (or equivalently eq. (15)) results in an algebraic generalized Hermitian eigenvalue problem that can be written as

$$\mathbf{H}^{\mathbf{k}} \mathbf{U}^{\mathbf{k}} = \mathbf{M} \mathbf{U}^{\mathbf{k}} \mathbf{\Lambda}^{\mathbf{k}} \quad (39)$$

where $\mathbf{U}^{\mathbf{k}}$ is the matrix with n^{th} column formed by the 2-component complex linear combination coefficients corresponding to spinor wavefunction of index n . Hence,

the matrix entries $U_{2I+\alpha,n}^{\mathbf{k}}$ correspond to $u_{n\mathbf{k}}^{I,\alpha}$ as defined in eq. (38). The discretized Hamiltonian matrix $\mathbf{H}^{\mathbf{k}} = \mathbf{H}^{\mathbf{k},\text{loc}} + \mathbf{H}^{\mathbf{k},\text{nloc}}$, and the FE basis overlap matrix \mathbf{M} are $2M^{h,p} \times 2M^{h,p}$ complex Hermitian matrices. The local part of this Hamiltonian, $\mathbf{H}^{\mathbf{k},\text{loc}}$, can now be written as

$$\begin{aligned} \mathbf{H}_{2I+\alpha,2J+\beta}^{\mathbf{k},\text{loc}} &= \\ &\int_{\Omega_p} \left(\left[\frac{1}{2} \nabla N_I^{h,p}(\mathbf{r}) \cdot \nabla N_J^{h,p}(\mathbf{r}) - i N_I^{h,p}(\mathbf{r}) \mathbf{k} \cdot \nabla N_J^{h,p}(\mathbf{r}) \right. \right. \\ &\quad \left. \left. + \frac{|\mathbf{k}|^2}{2} N_I^{h,p}(\mathbf{r}) N_J^{h,p}(\mathbf{r}) + V_{\text{eff}}(\mathbf{r}) N_I^{h,p}(\mathbf{r}) N_J^{h,p}(\mathbf{r}) \right] \delta_{\alpha\beta} \right. \\ &\quad \left. + \sum_{d=x,y,z} \left[B_{\text{xc}}^d(\mathbf{r}) N_I^{h,p}(\mathbf{r}) N_J^{h,p}(\mathbf{r}) \right] \sigma_{\alpha\beta}^d \right) d\mathbf{r} \end{aligned} \quad (40)$$

where I, J are the FE basis function indices ranging from 0 to $M^{h,p} - 1$ and α, β are the spin indices taking values of $\{0, 1\}$. The non-local part of the FE discretized Hamiltonian, $\mathbf{H}^{\mathbf{k},\text{nloc}}$ can be written as

$$\mathbf{H}_{2I+\alpha,2J+\beta}^{\mathbf{k},\text{nloc}} = \sum_a \sum_{\chi\chi'} P_{I\chi}^{a,\mathbf{k}} D_{\alpha\beta}^{\gamma_a,\chi,\chi'} \sigma_{J\chi}^{a,\mathbf{k}*} \quad (41)$$

where the $M^{h,p} \times n_{\text{pj}}^a$ matrices $\mathbf{P}^{a,\mathbf{k}}$, with n_{pj}^a denoting the number of non-local projectors for atom a , are defined as

$$P_{I\chi}^{a,\mathbf{k}} = \int_{\Omega_p} \sum_q e^{-i\mathbf{k} \cdot (\mathbf{r} - \mathbf{L}_q)} p_{\chi}^a(\mathbf{r} - \mathbf{L}_q) N_I^{h,p}(\mathbf{r}) d\mathbf{r} \quad (42)$$

Finally, the FE basis overlap matrix is defined by

$$M_{2I+\alpha,2J+\beta} = \delta_{\alpha\beta} \int_{\Omega_p} N_I^{h,p}(\mathbf{r}) N_J^{h,p}(\mathbf{r}) d\mathbf{r} \quad (43)$$

To evaluate the above integrals, we consider partitioning of the simulation domain Ω_p into non-overlapping hexahedral cells, $\Omega^{(e)}$. Denoting E to be the number of FE cells, we have $\Omega_p = \bigcup_{e=1}^E \Omega^{(e)}$, and further, within each cell $\Omega^{(e)}$, we employ n_p^3 three-dimensional (3D) Lagrange polynomial basis functions that are tensor products of 1D Lagrange polynomials of degree p ($n_p = p + 1$) constructed over Gauss Lobatto Legendre (GLL) nodal points, where n_p denotes the number of these nodal points in each spatial direction [63]. This ensures that a given Lagrange polynomial basis function $N_I^{h,p}(\mathbf{r})$ centered at a FE nodal point I is non-zero in a given element $\Omega^{(e)}$ if and only if $I \in \Omega^{(e)}$. Consequently, the integrals over Ω_p in eqs. (40), (42) and (43) are decomposed into integrals over individual cells $\Omega^{(e)}$ and Gauss Legendre quadrature rules are employed to evaluate these integrals over a reference cell $[-1, 1]^3$ mapped from $\Omega^{(e)}$ as is done traditionally in finite-element based methods [64]. To this end, we have

$$\int_{\Omega_p} d\mathbf{r} \rightarrow \sum_e \int_{\Omega^{(e)}} d\mathbf{r} \rightarrow \sum_e \sum_q w_q J^{(e)} \Big|_{\mathbf{r}_q^{(e)}} \quad (44)$$

where $J^{(e)}$ is the determinant of $\mathbf{J}^{(e)}$, the Jacobian of the map from the FE cell $\Omega^{(e)}$ to the reference cell, and w_q and $\mathbf{r}_q^{(e)}$ denote the Gauss-Legendre quadrature weights and sampling points constructed as a tensor product of 1D Gauss-Legendre quadrature rules of order n_q . The order of the quadrature rule is chosen such that the quadrature errors are of higher order than that of the finite-element discretization error incurred in the ground-state energies.

1. Evaluation of effective potential

We now begin with a discussion on the evaluation of the exchange-correlation terms within the framework of noncollinear magnetism (V_{xc} and \mathbf{B}_{xc}) as it requires non-trivial considerations in the finite-element setting, especially for the case of GGA functionals as described below:

a. Evaluation of V_{xc} and B_{xc} : Under the locally collinear approximation [56], the functional derivatives of the exchange-correlation energy can be written as

$$V_{xc} = f^+ - \nabla \cdot \mathbf{g}^+ \quad (45)$$

$$\mathbf{B}_{xc} = \hat{\mathbf{m}} (f^- - \nabla \cdot \mathbf{g}^-) \quad (46)$$

where $\hat{\mathbf{m}}$ is the direction vector of the magnetization density given by $\hat{\mathbf{m}} = \mathbf{m}/|\mathbf{m}|$. The scalar fields f^\pm and the vector fields \mathbf{g}^\pm are given by

$$f^\pm = \frac{1}{2} \left(\frac{\partial f^{xc}}{\partial \rho^\uparrow} \pm \frac{\partial f^{xc}}{\partial \rho^\downarrow} \right) \quad (47)$$

$$\mathbf{g}^\pm = \frac{\partial f^{xc}}{\partial \gamma_0} \nabla \rho^\uparrow \pm \frac{\partial f^{xc}}{\partial \gamma_2} \nabla \rho^\downarrow + \frac{1}{2} \frac{\partial f^{xc}}{\partial \gamma_1} (\nabla \rho^\downarrow \pm \nabla \rho^\uparrow) \quad (48)$$

From eqs. (45) to (48), we see that the evaluation of the exchange-correlation potentials requires the computation of Laplacians of the charge densities, which can lead to numerical difficulties [61]. Furthermore, these numerical issues are compounded by the fact that the C^0 continuous finite-element basis employed to discretize the electronic fields in the current work does not allow for the computation of higher-order derivatives accurately. However, as can be seen from eq. (40), one only requires the evaluation of integrals involving exchange-correlation terms and hence, a typical strategy is to employ the divergence theorem to recast this integral in terms of only the gradients of the electronic fields in contrast to Laplacians as

in eqs. (47) and (48). To this end, we have

$$\int_{\Omega_p} V_{xc} N_I^{h,p} N_J^{h,p} d\mathbf{r} = \int_{\Omega_p} \left(f^+ N_I^{h,p} N_J^{h,p} + \nabla \cdot \left(N_I^{h,p} N_J^{h,p} \right) \cdot \mathbf{g}^+ \right) d\mathbf{r} \quad (49)$$

$$\int_{\Omega_p} \mathbf{B}_{xc} N_I^{h,p} N_J^{h,p} d\mathbf{r} = \int_{\Omega_p} \left(f^- \hat{\mathbf{m}} N_I^{h,p} N_J^{h,p} + \nabla \cdot \left(\hat{\mathbf{m}} N_I^{h,p} N_J^{h,p} \right) \cdot \mathbf{g}^- \right) d\mathbf{r} \quad (50)$$

While such an approach is satisfactory in the case of spin-unpolarized and collinear-spin calculations and has been employed in prior works [24, 39], it is not viable in the current case of noncollinear framework as this approach requires the evaluation of gradient of the magnetization unit-vector ($\nabla \hat{\mathbf{m}}$), which causes the integral in eq. (50) to become unbounded when $\mathbf{m} = 0$. In order to avoid these issues, we resort to White and Bird [67] formalism where the authors prescribe an alternate approach to compute the exchange-correlation potentials for gradient-corrected functionals in the case of plane-wave basis. Extensions of this approach to other basis sets involving atomic-orbital basis, finite-difference techniques can be found in [27, 68, 69]. We now propose an extension to the White and Bird approach for evaluating V_{xc} and \mathbf{B}_{xc} in the case of GGA functionals arising in noncollinear magnetism within the framework of finite-element discretization. To evaluate the integrals in eq. (40) using eq. (44), we need to compute V_{xc} and \mathbf{B}_{xc} at the quadrature points and the following discussion provides a prescription to do so.

To this end, we begin with the integral involved in computing exchange-correlation energy (E_{xc}) in eq. (11) and use eq. (44) to recast it into a discrete form given by

$$\tilde{E}_{xc} = \sum_e \sum_{q'} w_{q'} J^{(e)} f_{xc}(\rho^\uparrow, \rho^\downarrow, \gamma_0, \gamma_1, \gamma_2) \Big|_{\mathbf{r}_q^{(e)}}. \quad (51)$$

Subsequently, following the prescription in [27, 68, 69], we derive the expressions for the exchange-correlation terms V_{xc} and \mathbf{B}_{xc} at quadrature points as

$$V_{xc}(\mathbf{r}_q^{(e)}) = \frac{1}{w_q J^{(e)}} \frac{\delta \tilde{E}_{xc}}{\delta \rho(\mathbf{r}_q^{(e)})} \quad (52)$$

$$\mathbf{B}_{xc}(\mathbf{r}_q^{(e)}) = \frac{\hat{\mathbf{m}}(\mathbf{r}_q^{(e)})}{w_q J^{(e)}} \frac{\delta \tilde{E}_{xc}}{\delta |\mathbf{m}|(\mathbf{r}_q^{(e)})} \quad (53)$$

We now treat the exchange-correlation energy strictly as a functional of charge density ρ and the magnitude of the magnetization density $|\mathbf{m}|$ by defining $\nabla \rho$ and $\nabla |\mathbf{m}|$ as functionals of ρ and $|\mathbf{m}|$ respectively, at the quadrature points. To this end, the exchange-correlation terms V_{xc}

and \mathbf{B}_{xc} in eqs. (52) and (53) can now be recast as

$$V_{\text{xc}}(\mathbf{r}_q^{(e)}) = f^+(\mathbf{r}_q^{(e)}) + \sum_{q'} \frac{w_{q'}}{w_q} \mathbf{g}^+(\mathbf{r}_{q'}^{(e)}) \cdot \frac{\delta \nabla \rho(\mathbf{r}_{q'}^{(e)})}{\delta \rho(\mathbf{r}_q^{(e)})} \quad (54)$$

$$\mathbf{B}_{\text{xc}}(\mathbf{r}_q^{(e)}) = \hat{\mathbf{m}}(\mathbf{r}_q^{(e)}) \left(f^-(\mathbf{r}_q^{(e)}) + \sum_{d=x,y,z} \sum_{q'} \frac{w_{q'}}{w_q} \hat{m}_d(\mathbf{r}_{q'}^{(e)}) \mathbf{g}^-(\mathbf{r}_{q'}^{(e)}) \cdot \frac{\delta \nabla m_d(\mathbf{r}_{q'}^{(e)})}{\delta |\mathbf{m}|(\mathbf{r}_q^{(e)})} \right) \quad (55)$$

where we have used the relation $\nabla |\mathbf{m}| = \sum_{d=x,y,z} \hat{m}_d \nabla m_d$.

We note that the above expressions in eqs. (54) and (55) require the evaluation of the following functional derivatives

$$\frac{\delta \nabla \rho(\mathbf{r}_{q'}^{(e)})}{\delta \rho(\mathbf{r}_q^{(e)})} \quad \frac{\delta \nabla m_d(\mathbf{r}_{q'}^{(e)})}{\delta |\mathbf{m}|(\mathbf{r}_q^{(e)})} \quad (56)$$

where the indices q and q' are over the Gauss-Legendre quadrature points used to evaluate eq. (51). To evaluate these functional derivatives, we note that within any given FE-cell the charge density and the magnetization density computed using eqs. (4), (5) and (38) lie in the space spanned by 3D tensor-structured polynomials constructed from 1D Lagrange polynomials of order $2n_p$. Consequently, we now define Lagrange polynomial basis $\bar{N}_q^{(e)}(\mathbf{r}) : 0 \leq q < n_q^3$ constructed over the Gauss-Legendre quadrature points within each FE-cell $\Omega^{(e)}$ with $n_q \geq 2n_p$ so that the total charge density (ρ) and the magnetization density ($\mathbf{m} = (m_x, m_y, m_z)$) computed using eqs. (4), (5) and (38) can be represented exactly using the basis defined by $\bar{N}_q^{(e)}(\mathbf{r})$ allowing us to express

$$\rho(\mathbf{r}) = \sum_q \rho(\mathbf{r}_q^{(e)}) \bar{N}_q^{(e)}(\mathbf{r}) \quad \forall \mathbf{r} \in \Omega^{(e)} \quad (57)$$

$$m_d(\mathbf{r}) = \sum_q m_d(\mathbf{r}_q^{(e)}) \bar{N}_q^{(e)}(\mathbf{r}) \quad \forall \mathbf{r} \in \Omega^{(e)} \quad (58)$$

and correspondingly the gradients

$$\nabla \rho(\mathbf{r}) = \sum_q \rho(\mathbf{r}_q^{(e)}) \nabla \bar{N}_q^{(e)}(\mathbf{r}) \quad (59)$$

$$\nabla m_d(\mathbf{r}) = \sum_q m_d(\mathbf{r}_q^{(e)}) \nabla \bar{N}_q^{(e)}(\mathbf{r}) \quad (60)$$

the required functional derivatives can now be evaluated as

$$\frac{\delta \nabla \rho(\mathbf{r}_{q'}^{(e)})}{\delta \rho(\mathbf{r}_q^{(e)})} = \nabla \bar{N}_q^{(e)}(\mathbf{r}_{q'}^{(e)}) \quad (61)$$

$$\frac{\delta \nabla m_d(\mathbf{r}_{q'}^{(e)})}{\delta |\mathbf{m}|(\mathbf{r}_q^{(e)})} = \hat{m}_d(\mathbf{r}_q^{(e)}) \nabla \bar{N}_q^{(e)}(\mathbf{r}_{q'}^{(e)}) \quad (62)$$

where we have used the relation $m_d = |\mathbf{m}| \hat{m}_d$.

2. Evaluation of V_{el} :

The total electrostatic potential (V_{el}) is evaluated as the solution of the Poisson problem given by eq. (9). We now define $N_I^{h,p_{\text{el}}}(\mathbf{r}) : 0 \leq I < M^{h,p_{\text{el}}}$ as the 3D tensor-structured FE polynomial basis constructed from 1D Lagrange polynomials of degree p_{el} defined over Gauss Lobatto Legendre (GLL) nodal points [63], generated using the same FE triangulation \mathcal{T}^h used for the solution of eq. (22). In this framework, the FE-discretized Poisson problem (eq. (9)) reduces to a system of equations given by

$$\mathbf{K} \mathbf{V}_{\text{el}} = \boldsymbol{\rho} \quad (63)$$

Where \mathbf{K} is the FE discretized Laplacian operator given by

$$K_{IJ} = \int \nabla N_I^{h,p_{\text{el}}}(\mathbf{r}) \cdot \nabla N_J^{h,p_{\text{el}}}(\mathbf{r}) d\mathbf{r} \quad (64)$$

and the $M^{h,p_{\text{el}}} \times 1$ vector \mathbf{V}_{el} consists of the basis coefficients of the discrete electrostatic potential (V_{el}) while the $M^{h,p_{\text{el}}} \times 1$ vector $\boldsymbol{\rho}$ is given by

$$\rho_I = \int \rho(\mathbf{r}) N_I^{h,p_{\text{el}}}(\mathbf{r}) d\mathbf{r} \quad (65)$$

The solution to eq. (63) is computed using a conjugate-gradient method.

B. Self-Consistent Field Iteration

We now discuss the numerical strategies used to solve the discretized nonlinear generalized eigenvalue problem described by eqs. (39) to (43). Towards this goal, we employ the self-consistent field procedure commonly adopted in DFT calculations [24, 39, 70–73] to convert the nonlinear eigenvalue problem to a sequence of linear eigenvalue problems. Each of these linear eigenvalue problems is then solved by making use of a modified Chebyshev filtered subspace iteration (ChFSI) procedure [74]. As the nonlinear eigenvalue problems for each wavevector \mathbf{k} are mutually independent, we omit the index \mathbf{k} in the subsequent sections for notational convenience.

1. Density Mixing

The nonlinear eigenvalue problem within the framework of noncollinear magnetism can be formulated as a fixed point iteration problem as

$$F[(\rho, \mathbf{m})] = (\rho, \mathbf{m}) \quad (66)$$

where map $F[(\rho_{\text{in}}, \mathbf{m}_{\text{in}})] = (\rho_{\text{out}}, \mathbf{m}_{\text{out}})$ represents the computation of V_{eff} and \mathbf{B}_{xc} using $(\rho_{\text{in}}, \mathbf{m}_{\text{in}})$, solving the

FE-discretized eigenvalue problem given by eq. (39) and computing $(\rho_{out}, \mathbf{m}_{out})$ using eqs. (4), (5) and (38). In order to accelerate the convergence of the self-consistent field iteration procedure, we employ the Anderson mixing scheme [75, 76], which computes the input densities for the next iteration as linear combinations of the previous i input densities and residuals.

$$(\rho_{in}^{i+1}, \mathbf{m}_{in}^{i+1}) = \sum_{j=1}^i b_{i,j} (\rho_{in}^j, \mathbf{m}_{in}^j) + \alpha b_{i,j} (\rho_{res}^j, \mathbf{m}_{res}^j) \quad (67)$$

where $(\rho_{res}^j, \mathbf{m}_{res}^j) = F \left[(\rho_{in}^j, \mathbf{m}_{in}^j) \right] - (\rho_{in}^j, \mathbf{m}_{in}^j)$ and $b_{i,j}$ are chosen such that $\sum_{j=1}^i b_{i,j} = 1$ and

$$\left\| \sum_{j=1}^i b_{i,j} (\rho_{res}^j, \mathbf{m}_{res}^j) \right\| \quad (68)$$

is minimized where $\|\cdot\|$ is the norm induced by the inner product defined as

$$\langle (\rho_1, \mathbf{m}_1), (\rho_2, \mathbf{m}_2) \rangle = \frac{1}{2} \left(\int_{\Omega_p} \rho_1 \rho_2 + \int_{\Omega_p} \mathbf{m}_1 \cdot \mathbf{m}_2 \right) \quad (69)$$

RPA based preconditioners such as the Kerker [77] or the Resta preconditioner [78] are applied to the total charge density residuals, $\rho_{res} \leftarrow K \rho_{res}$ where K denotes the action of the preconditioner.

2. Subspace iteration for linear eigenproblem

In order to solve the generalized Hermitian eigenvalue problem (GHEP) described by eq. (39), we employ a Chebyshev filtered subspace iteration (ChFSI) procedure that naturally allows the use of filtered subspace rich in desired eigenvectors of a given SCF iteration to a subsequent iteration progressively improving the convergence towards the self-consistent solution. Furthermore, we note that the ChFSI method is well-suited for modern high-performance computing architectures and has been employed in prior works involving the solution of standard eigenvalue problems arising in real-space DFT calculations [24, 25, 79, 80]. To solve GHEP in eq. (39) using ChFSI, we first seek to amplify the eigenspace of interest by constructing a Chebyshev polynomial filter corresponding to the matrix $\mathbf{M}^{-1}\mathbf{H}$ that has the same eigenspace as $\mathbf{H}\mathbf{U} = \mathbf{M}\mathbf{U}\mathbf{\Lambda}$. Towards this, we efficiently evaluate \mathbf{M}^{-1} , a $2M^{h,p} \times 2M^{h,p}$ matrix by employing Gauss-Lobatto-Legendre (GLL) quadrature rules coincident with the finite-element nodes of the spectral finite-elements employed in this work, rendering \mathbf{M} diagonal. Denoting this diagonal matrix as \mathbf{M}_D , we now seek to construct the subspace rich in the desired eigenvectors by first scaling and shifting the matrix $\tilde{\mathbf{H}} = \mathbf{M}_D^{-1}\mathbf{H}$ so that

the unwanted spectrum ($[\lambda_T, \lambda_{max}]$) is mapped to $[-1, 1]$ where λ_T and λ_{max} denote the upper bounds of wanted and unwanted spectrum respectively. Subsequently, the filtered vectors are evaluated using the three-term recurrence relation of the Chebyshev polynomials as

$$\mathbf{X}_k = T_k(\tilde{\mathbf{H}})\mathbf{X} \quad \forall k = 0, 1, 2, \dots, s$$

$$\text{where } T_{k+1}(\tilde{\mathbf{H}}) = 2\tilde{\mathbf{H}}T_k(\tilde{\mathbf{H}}) - T_{k-1}(\tilde{\mathbf{H}}) \quad (70)$$

where \mathbf{X} is the initial guess of the eigenvectors and T_k is the scaled Chebyshev polynomial of degree k , and s denotes the choice of the Chebyshev polynomial degree used for filtering the vectors in a given SCF iteration. The above recurrence relation involving the scaled Hamiltonian exploits the exponential growth of Chebyshev polynomials outside of $[-1, 1]$ to amplify the desired spectrum $[\lambda_{min}, \lambda_T]$ where λ_{min} denotes the lower bound of the wanted spectrum. Values of λ_{min} and λ_{max} are estimated based on the Lanczos method with a generalized variant [81] while a good approximation to the value of λ_T is estimated based on the highest generalized Rayleigh quotient of $\tilde{\mathbf{H}}$ of the previous SCF iteration.

In the conventional Chebyshev filtering algorithm as described above, the predominant computational cost is the evaluation of Hamiltonian times vector products, $\mathbf{H}\mathbf{X}_k$. To this end, we reformulate the filtering step¹ by substituting these products with Hamiltonian-times residual products, and as we approach convergence, these eigenproblem residuals progressively become smaller. Consequently, it becomes viable to compute these Hamiltonian times residual products in lower precision without compromising accuracy, thus improving the computational efficiency [74].

Once we obtain the filtered subspace $\mathbf{X}_s = T_s(\tilde{\mathbf{H}})\mathbf{X}$, we use the Rayleigh-Ritz projection step to obtain the desired eigenvectors and eigenvalues. In light of this, we solve the subspace-projected eigenvalue problem defined by

$$\mathbf{X}_s^\dagger \mathbf{H} \mathbf{X}_s \mathbf{Q}_s = \mathbf{X}_s^\dagger \mathbf{M} \mathbf{X}_s \mathbf{Q}_s \mathbf{\Lambda}_s \quad (71)$$

where \mathbf{Q}_s and $\mathbf{\Lambda}_s$ are the eigenvectors and eigenvalues of the above $T \times T$ generalized eigenvalue problem. The new estimates for the eigenvectors and eigenvalues can be obtained as

$$\mathbf{U} = \mathbf{X}_s \mathbf{Q}_s \quad \mathbf{\Lambda} = \mathbf{\Lambda}_s \quad (72)$$

This process of Chebyshev filtering, followed by a Rayleigh-Ritz step, is repeated till a desired residual tolerance is reached for a given SCF iteration.

¹ Manuscript under preparation

IV. NUMERICAL IMPLEMENTATION STRATEGIES

In this section, we discuss the computationally efficient approaches underlying our numerical implementation that accelerate the finite-element (FE) based solution procedure described in section III. In particular, we describe the two-grid strategy employed to accelerate the SCF procedure and further highlight the key numerical aspects involved in evaluating the action of FE discretized Hamiltonian on the trial subspace of complex spinors, the computationally intensive step of the linear eigensolver within the framework of noncollinear magnetism.

A. Two-grid strategy

At the beginning of the self-consistent field (SCF) iteration where the electronic fields ρ and \mathbf{m} are far away from the self-consistent solution, one does not need to evaluate $F[(\rho, \mathbf{m})]$ in eq. (66) accurately, and leveraging this, we solve the linear eigenvalue problem approximately using a lower FE interpolating polynomial order $p-1$ in the initial SCF iterations instead of using p . We refer to this approach as the ‘‘Two-grid strategy’’ and here, the discretized 2-component complex spinors are expressed as

$$\mathbf{u}_{nk}^{h,p-1}(\mathbf{r}) = \sum_I \mathbf{u}_{nk}^I N_I^{h,p-1}(\mathbf{r}) \quad (73)$$

where $N_I^{h,p-1}(\mathbf{r}) : 0 \leq I < M^{h,p-1}$ are the 3D tensor-structured FE polynomial basis constructed from 1D Lagrange polynomials of degree $p-1$ defined over Gauss Lobatto Legendre (GLL) nodal points [63], generated using the nodes of the same FE triangulation \mathcal{T}^h defined in section III A. Consequently the FE discretized eigenvalue problem defined by eq. (39) and the FE discretized matrices defined by eqs. (40) to (43) are also computed using $N_I^{h,p-1}(\mathbf{r})$ instead of $N_I^{h,p}(\mathbf{r})$ resulting in an eigenvalue problem of reduced dimension ($M^{h,p-1} < M^{h,p}$) that is computationally cheaper to solve. We perform the self-consistent iteration using this reduced-order discretization until a chosen tolerance of charge and magnetization density residuals (in the norm induced by the inner product defined by eq. (69)) is achieved. In all the numerical calculations reported in this work, this tolerance is typically chosen higher than the value chosen for the convergence of the complete self-consistent iteration.

B. Action of FE discretized Hamiltonian

We note that the action of the FE discretized Hamiltonian on a trial subspace encountered in the ChFSI procedure described previously involves the computationally

intensive step of evaluating the matrix-multivector product $\mathbf{H}\mathbf{Y}$ that entails the multiplication of a sparse-matrix (\mathbf{H}) with a dense-matrix (\mathbf{Y}). It has been noted previously that a direct sparse-matrix times dense-matrix (spMM) is computationally expensive than other methods available in the FE literature [24, 25, 38, 39, 82–84]. We adopt one such method by extending the strategy to the FE discretized matrices arising in the noncollinear and the SOC framework described here, where the spMM operation is recast into multiple smaller dense-matrix times dense-matrix products that have high arithmetic intensity. Key ideas are described below.

1. Cell-level Hamiltonian matrices:

Towards the goal of recasting to small dense matrix-matrix products, we now define dense FE cell-level matrix $\mathbf{H}^{\text{loc}(e)}$ of size $2n_p^3 \times 2n_p^3$ corresponding to the local part of the FE discretized Hamiltonian \mathbf{H}^{loc} defined in eq. (40) in the following manner

$$\mathbf{H}^{\text{loc}} = \sum_e \mathcal{R}^{(e)T} \mathbf{H}^{\text{loc}(e)} \mathcal{R}^{(e)} \quad (74)$$

where $\mathcal{R}^{(e)}$ is a $2M^{h,p} \times 2n_p^3$ Boolean sparse matrix which extracts the basis coefficients, \mathbf{u}_{nk}^I in eq. (38), corresponding to an FE-cell $\Omega^{(e)}$, i.e. $I \in \Omega^{(e)}$ and is commonly referred to as the restriction matrix.

In this framework the cell-level non-local projector matrices $\mathbf{P}^{a(e)}$ of size $2n_p^3 \times 2n_{\text{pj}}^a$ corresponding to the FE discretized projector matrices defined by eq. (42) can be written as

$$\begin{bmatrix} \mathbf{P}^a & 0 \\ 0 & \mathbf{P}^a \end{bmatrix} = \sum_e \mathcal{R}^{(e)T} \mathbf{P}^{a(e)} \quad (75)$$

Furthermore, we define the $2n_{\text{pj}}^a \times 2n_{\text{pj}}^a$ matrix Δ^{γ_a} corresponding to the non-local pseudopotential coefficients present in the non-local part of the Hamiltonian (eq. (41)) as

$$\Delta_{2\chi+\alpha, 2\chi'+\beta}^{\gamma_a} = D_{\alpha\beta}^{\gamma_a, \chi, \chi'} \quad (76)$$

The cell-level local Hamiltonian matrices ($\mathbf{H}^{\text{loc}(e)}$) and the non-local projector matrices $\mathbf{P}^{a(e)}$ are computed as

$$\begin{aligned} \mathbf{H}_{2I+\alpha, 2J+\beta}^{\text{loc}(e)} &= \int_{\Omega^{(e)}} \left(\left[\frac{1}{2} \nabla N_I^{h,p}(\mathbf{r}) \cdot \nabla N_J^{h,p}(\mathbf{r}) \right. \right. \\ &\quad \left. \left. + V_{\text{eff}}(\mathbf{r}) N_I^{h,p}(\mathbf{r}) N_J^{h,p}(\mathbf{r}) \right] \delta_{\alpha\beta} \right. \\ &\quad \left. + \sum_{d=x,y,z} \left[B_{\text{xc}}^d(\mathbf{r}) N_I^{h,p}(\mathbf{r}) N_J^{h,p}(\mathbf{r}) \right] \sigma_{\alpha\beta}^d \right) d\mathbf{r} \quad (77) \end{aligned}$$

$$\mathbf{P}_{2I+\alpha, 2\chi+\beta}^{a(e)} = \delta_{\alpha\beta} \int_{\Omega^{(e)}} p_{\chi}^a(\mathbf{r}) N_I^{h,p}(\mathbf{r}) d\mathbf{r} \quad (78)$$

In order to evaluate these integrals we define the Lagrange polynomial basis functions, \tilde{N}_I , defined on 3D tensor structured Gauss-Legendre-Lobatto quadrature points, $\tilde{\mathbf{r}}_q$ in the reference cell $\tilde{\Omega} = [-1, 1]^3$. In order to elucidate the methodology followed for the evaluation of the integrals in eqs. (77) and (78) we consider the term $\int V_{\text{eff}} N_I^{h,p} N_J^{h,p}$, in terms of the basis functions in the reference cell this integral can be written as

$$\int_{\Omega^{(e)}} V_{\text{eff}}(\mathbf{r}) N_I^{h,p}(\mathbf{r}) N_J^{h,p}(\mathbf{r}) d\mathbf{r} \quad (79)$$

$$= \int_{\tilde{\Omega}} V_{\text{eff}}(\mathbf{r}(\tilde{\mathbf{r}})) \tilde{N}_I^{h,p}(\tilde{\mathbf{r}}) \tilde{N}_J^{h,p}(\tilde{\mathbf{r}}) J^{(e)} d\tilde{\mathbf{r}} \quad (80)$$

$$= \sum_q V_{\text{eff}}(\mathbf{r}_q) \tilde{N}_I^{h,p}(\tilde{\mathbf{r}}_q) \tilde{N}_J^{h,p}(\tilde{\mathbf{r}}_q) J^{(e)} w_q \quad (81)$$

Defining $\tilde{\mathbf{N}}$ to be the $n_p^3 \times n_q^3$ matrix whose elements are given by $\tilde{N}_{Iq} = \tilde{N}_I(\mathbf{r}_q)$ and \mathbf{V}^{eff} to be the $n_q^3 \times n_q^3$ diagonal matrix whose elements are given by $V_{qq'}^{\text{eff}} = \delta_{qq'} w_q J^{(e)} V_{\text{eff}}(\mathbf{r}_q)$, the integral can now be written as

$$\int_{\Omega^{(e)}} V_{\text{eff}}(\mathbf{r}) N_I^{h,p}(\mathbf{r}) N_J^{h,p}(\mathbf{r}) d\mathbf{r} = \mathbf{V}_{IJ} \quad (82)$$

where the matrix \mathbf{V} is given by

$$\mathbf{V} = (\tilde{\mathbf{N}} \circ \mathbf{V}^{\text{eff}}) \tilde{\mathbf{N}}^T \quad (83)$$

where \circ represents the Hadamard product of two matrices. The matrix \mathbf{V} can now be efficiently evaluated using standard level-3 BLAS functions and their strided/batched variants. The other integrals in eqs. (77) and (78) are also evaluated using a similar methodology.

2. FE discretized matrix multivector product

The matrix multivector product $\mathbf{Y} = \mathbf{H}\mathbf{X}$ required in eq. (70) can then be evaluated using these FE-cell level dense matrices and the FE-cell level multivectors [24, 39, 83]. This strategy comprises of the following steps :

1. Precompute the FE-cell level operator matrices $\mathbf{H}^{\text{loc}(e)}$ and $\mathbf{P}^{a(e)}$.
2. Extraction of the FE-cell level multivectors $\mathbf{Y}^{(e)}$ using the restriction matrix, i.e., $\mathbf{X}^{(e)} = \mathcal{R}^{(e)}\mathbf{X}$ $\forall e = 1, 2, \dots, E$.
3. FE-cell level evaluation of the matrix multivector products

$$\mathbf{Y}^{(e)} = \mathbf{H}^{\text{loc}(e)} \mathbf{X}^{(e)} + \sum_a \mathbf{P}^{a(e)} \Delta \gamma_a \sum_{e'} \mathbf{P}^{a(e')\dagger} \mathbf{X}^{(e')} \quad (84)$$

This operation is done using BLAS routines [85] for dense matrix-matrix multiplication.

4. Assembly of the global multivector \mathbf{Y} using the restriction matrix, i.e., $\mathbf{Y} = \sum_e^E \mathcal{R}^{(e)T} \mathbf{Y}^{(e)}$

V. RESULTS AND DISCUSSION

We now present comprehensive studies demonstrating the accuracy, performance and parallel scalability of the proposed computational approach (NCSOC-DFT-FE) on model benchmark systems involving periodic, semi-periodic and non-periodic boundary conditions. Accuracy benchmarks involve comparisons of ground-state energies, magnetic anisotropy energies, volume integral of magnetization densities, vertical ionization potentials, spin textures, band-structures with plane-wave-based DFT calculations using Quantum espresso (QE) [73, 86, 87] for various representative examples considered in this work. Furthermore, on CPU architectures, performance comparisons of NCSOC-DFT-FE with respect to plane-wave DFT calculations involving noncollinear magnetism and spin-orbit coupling have been carried out for system sizes ranging from ~ 3000 to 15000 electrons. To this end, we employ two metrics to compare the performance: (i) computational cost per SCF iteration ² (η) in node-hrs, and (ii) minimum wall time per SCF iteration ³ (τ^{min}) in secs. Additionally, we present performance benchmarks of our method on GPU architectures for these large-scale systems. Finally, we showcase the parallel scalability of NCSOC-DFT-FE on multi-node CPU and GPU architectures on representative periodic and semi-periodic material systems. All simulations involved in the accuracy benchmarking are performed on KNL CPU nodes on Nurion⁴, and performance benchmarking studies were performed both on CPU nodes of Nurion and GPU nodes of Frontier⁵. Note that we do not show GPU benchmarks of QE on Frontier as it does not yet fully support AMD GPUs [88].

Unless otherwise specified, all the DFT calculations reported in this work utilize the PBE functional [89] for

² η is obtained by multiplying the minimum number of compute nodes required to fit a given problem with the average wall-time per SCF iteration

³ τ^{min} is obtained by computing the average wall time per SCF by increasing the number of compute nodes till the time does not change significantly or starts increasing

⁴ Nurion is one of South Korea's fastest supercomputers stationed at KIST comprising of 8305 Intel Xeon KNL based CPU nodes (564,740 Cores) where each node consists of 68 cores (Intel Xeon Phi 7250 processor), 96 GB memory and Fat-tree topology based high-performance interconnect between all the nodes for fast MPI communication.

⁵ Frontier is the world's first exascale supercomputer stationed at ORNL comprising of 9408 AMD compute nodes with node containing 8 GPUs per node each having 64 GB of high-bandwidth memory

the exchange-correlation and fully relativistic optimized norm-conserving pseudopotentials (ONCV) [60] from the Pseudo-Dojo database [90]. All calculations were performed using Fermi-Dirac smearing with a smearing temperature of 500 K. The initial guess for magnetization density is chosen to be similar for both Quantum-Espresso and DFT-FE for all the calculations reported here. In the accuracy validation studies discussed in this work using NCSOC-DFT-FE, we employ refined finite element (FE) meshes with FE interpolating polynomial (p) of degree 6. These meshes are constructed such that the discretization error in ground-state energy is less than $\mathcal{O}(10^{-5})$ Ha/atom. Additionally, FE interpolating polynomial degree for electrostatics p_{el} and the quadrature integration rules are chosen such that the energy variation with respect to these parameters is an order of magnitude lower than this discretization error. Additionally, for mixing of the electron charge density ρ and magnetization density \mathbf{m} , we employ the n -stage Anderson mixing scheme [75] as discussed in the section III. In the case of plane wave calculations for accuracy validation studies using QE, the cutoff energy for wavefunctions `ecutwfc` is chosen so that the discretization error in ground-state energy is less than $\mathcal{O}(10^{-5})$ Ha/atom while simultaneously ensuring that the change in energy with respect to the cutoff energy for the electron charge density `ecutrho` is an order of magnitude lower. Further, the default mixing scheme is used in the case of QE. For metallic systems we use the Kerker preconditioner in both QE and NCSOC-DFT-FE. The structures of all the systems considered for accuracy benchmarks can be found in the supplementary material.

A. Non-periodic/Semi-periodic systems

In this subsection, we examine the case of fully non-periodic and semi-periodic systems for accuracy and performance benchmarking. In particular, we benchmark the accuracy of NCSOC-DFT-FE with QE by comparing the relaxed ground state energies of isolated systems and a semi-periodic system involving TMD bilayer. Furthermore, for some of these materials systems, we compute the vertical ionization potential and the volume integral of the magnetization density and compare the values with that obtained from QE. Following the accuracy validation study, we evaluated the performance of our implementation by comparing the computational cost in node hours and the minimum wall time of NCSOC-DFT-FE with QE, a widely used DFT code that uses the plane-wave basis. In this performance benchmarking study, we consider semi-periodic systems involving WTe₂ for various twist angles ranging from 180 atoms (3600 electrons) to 1032 atoms (20640 electrons). In NCSOC-DFT-FE, we apply homogeneous Dirichlet boundary conditions in the non-periodic directions for charge-neutral systems when solving for the electrostatic potential using eq. (63), and a suitable vacuum is used till the electronic fields decay to 0 in these

directions. In the plane-wave code QE, periodic boundary conditions (PBCs) are only admissible; hence, PBCs are employed using a suitable vacuum to minimize image-image interactions in non-periodic directions.

1. Accuracy benchmarking

In all the accuracy benchmarking studies of NCSOC-DFT-FE against QE reported here, we employ a kinetic energy cutoff (`ecutwfc`) of 75Ha in QE and a polynomial order of 6 with a finite-element mesh size of 0.8 Bohr in our method.

a. Energetics: Table I shows the comparison of total internal energies with QE, for a few representative gas-phase molecules from the GW-SOC81 benchmark set [91] involving heavy atoms (AgBr, AsI₃, (C₅H₅)₂Ru), 3-atom cluster of Chromium Cr₃ that exhibits a noncollinear magnetic state and bilayer WTe₂, a semi-periodic system that displays strong spin-orbit effects. In QE, for all the isolated systems simulated in this study, the Gamma point is used to sample the Brillouin zone. While simulating the semi-periodic system WTe₂ in QE, a shifted $4 \times 4 \times 1$ Monkhorst-Pack k-point grid is used for sampling the Brillouin zone [92] and periodic boundary conditions is applied in all 3-directions. In the case of NCSOC-DFT-FE, we employ periodic boundary conditions only in two directions spanning the plane of the bilayer, employing a shifted 4×4 Monkhorst-Pack k-point grid to sample the Brillouin zone.

System	QE (Ha)	NCSOC-DFT-FE (Ha)	Error (Ha/atom)
AgBr	-170.704020	-170.703937	4.1E-05
AsI ₃	-144.897928	-144.897902	6.6E-06
(C ₅ H ₅) ₂ Ru	-167.114509	-167.114752	1.2E-05
Cr ₃	-266.639352	-266.639406	1.8E-05
WTe ₂	-1143.255383	-1143.254923	3.8E-05

TABLE I. Accuracy benchmarks for total internal energy.

From table I, we observe an excellent match between NCSOC-DFT-FE and QE, and the errors between the approaches are well within chemical accuracy, validating the accuracy of our implementation. Furthermore, we also compare the volume integral of the magnitude of

System	QE(Bohr Magnetron)	NCSOC-DFT-FE (Bohr Magnetron)	Error (Bohr Magnetron)
Cr ₃	14.5367	14.5358	8.9E-04

TABLE II. Accuracy benchmarks for volume integral of the magnitude of magnetization density.

magnetization density for the 3-atom cluster of Cr_3 in table II and find a close correspondence between the two approaches compared here.

b. Vertical Ionization potentials: We now compare the vertical ionization potentials of a few gas-phase molecules from the GW-SOC81 benchmark set [91]. The vertical ionization potentials are computed using the Δ -SCF method

$$\text{VIP} = E(N_e - 1) - E(N_e) \quad (85)$$

where N_e is the number of valence electrons in the neutral molecule. To this end, we need to perform DFT calculations for charged molecules in both the approaches compared here. In the case of NCSOC-DFT-FE, we accomplish this by imposing multipole boundary conditions (up to the quadrupole term) on the total electrostatic potential while solving eq. (9) in a sufficiently large domain. In QE, we utilize the Makov-Payne correction [93] for isolated systems with sufficiently large supercells to avoid image interactions. Note that the treatment of the charged system is not equivalent to that of QE in our framework, and as such, we do not expect an exact match with it.

System	QE(eV)	NCSOC-DFT-FE (eV)	Experiment (eV)[91, 94]
AgBr	9.53	9.44	9.59
AsI ₃	8.58	8.62	9.00
(C ₅ H ₅) ₂ Ru	7.23	7.26	7.45

TABLE III. Accuracy benchmarks for vertical ionization potentials.

c. Spin textures: We also illustrate the spin texture of the Cr_3 system, which is known to exhibit a non-collinear magnetic Neel state due to geometric frustration. To this end, we consider a fully relaxed 3-atom cluster of Chromium (Cr_3); resulting in a Cr-Cr bond length of 4.86 Bohr and plot the spin-texture of the Neel state of Cr_3 in fig. 1 We note that the spin texture ob-

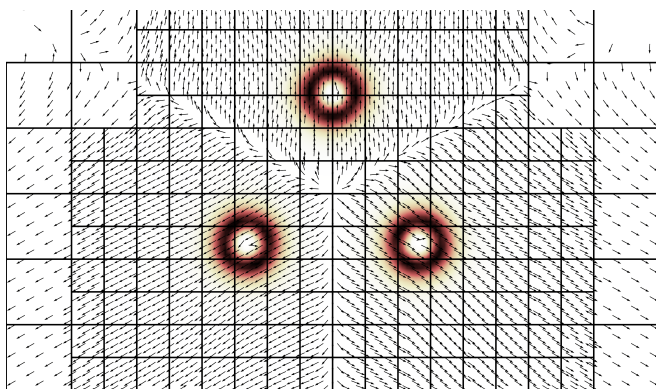


FIG. 1. Spin-textures for Cr_3

tained from our implementation is consistent with existing studies [35, 59].

2. Performance studies

We now discuss the performance of NCSOC-DFT-FE with QE by comparing the average CPU time per SCF iteration in terms of computational node-hrs (η_c) with increasing system sizes of a semi-periodic system solved to a similar level of accuracy. In particular, we consider the twisted bilayer WTe_2 for various twist angles. Incommensurate twisted bilayer WTe_2 requires simulation cells with a large number of atoms, and we consider twist angles ranging from 30 degrees to 12 degrees. To this end, semi-periodic pseudopotential DFT calculations involving noncollinear magnetism and spin-orbit coupling terms are conducted on $\text{W}_{60}\text{Te}_{120}$ (3600 electrons), $\text{W}_{116}\text{Te}_{232}$ (6960 electrons), $\text{W}_{168}\text{Te}_{336}$ (10080 electrons), $\text{W}_{228}\text{Te}_{456}$ (13680 electrons) and $\text{W}_{344}\text{Te}_{688}$ (20640 electrons). The structures were generated using the methodology described by He and Weng [5]. Table IV summarizes the twist angles and the configurations considered.

We employ the PBE functional [89] for the exchange-correlation and fully-relativistic optimized norm-conserving pseudopotentials (ONCV) [60] in the SG15 database [91]. In NCSOC-DFT-FE, we use the degree of FE interpolating polynomial p to be 7 and a FE mesh size of 1.5 Bohr while we employ a kinetic energy cutoff (`ecutwfc`) of 55 Ry in QE. These discretization parameters are chosen so that the discretization error in the ground-state energies obtained in both NCSOC-DFT-FE and QE is $\sim \mathcal{O}(10^{-4})$ Ha/atom. Additionally, we perform a non-magnetic calculation with SOC in both NCSOC-DFT-FE and QE employing a vacuum of around 14 Bohr and 10 Bohr, respectively above and below the twisted bilayer system, ensuring that ground-state energies are converged up to $\mathcal{O}(10^{-5})$ Ha/atom with vacuum size. Periodic boundary conditions are applied in the two lattice vector directions spanning the plane of the bilayer, and homogeneous Dirichlet boundary conditions are applied on the electrostatic potential in the direction normal to the bilayer in NCSOC-DFT-FE. In the case of QE periodic boundary conditions are employed in all three directions and Gamma point sampling of the Brillouin zone is used.

Table (IV) reports the average CPU time per SCF iteration in terms of computational node-hrs (η_c) and the number of basis functions in NCSOC-DFT-FE and QE for various sizes of twisted bilayers of WTe_2 considered here. Further, we also report the average time per SCF iteration in terms of GPU node-hrs (η_g) in this table. From this table, we find that for system sizes $\sim 10,000$ electrons and above, NCSOC-DFT-FE becomes more efficient than QE and gains increase with system size on CPUs. This increase in computational gains is attributed to the need for using more processors to satisfy the peak memory requirement, where the efficient parallel scalability of NCSOC-DFT-FE provides the necessary advantage. Additionally, we estimate the computational complexity in the regime of $\sim 3000 - 20000$ electrons for NCSOC-DFT-FE

System	Electrons	Twist angle	QE # of basis fns.	QE Nurion CPU Node-hrs (η_c)	NCSOC-DFT-FE # of basis fns.	NCSOC-DFT-FE Nurion CPU Node-hrs (η_c)	NCSOC-DFT-FE Frontier GPU Node-hrs (η_g)
W ₆₀ Te ₁₂₀	3600	30°	298615	0.9	3215206	2.9	0.04
W ₁₁₆ Te ₂₃₂	6960	49°	577425	8.2	6509526	14.0	0.2
W ₁₆₈ Te ₃₃₆	10080	26°	836149	37.8	8978220	27.8	0.4
W ₂₂₈ Te ₄₅₆	13680	15.5°	1134763	102.6	11971630	56.7	0.9
W ₃₄₄ Te ₆₈₈	20640	12.3°	1711991	– ^a	17930753	223.5	3.0

^a We were unable to perform this computation due to memory limitations on KNL architectures

TABLE IV. Computational cost (η) comparison between NCSOC-DFT-FE and QE in node-hrs (discretization error $\sim 10^{-4}$ Ha/atom). η is computed from the minimum number of nodes required to fit a given material system and the average wall time taken per SCF iteration. **Case Study:** Twisted bilayers of WTe₂ with varying twist angles

from table (IV) and is found to be of $\mathcal{O}(N_e^{2.4})$ while for QE we observe it to be of $\mathcal{O}(N_e^{3.6})$. Hence, we expect to see further gains of NCSOC-DFT-FE over QE with increasing system size on CPUs. We further note from this table that we obtain significant computational efficiencies on GPUs using the proposed computational methodologies. In particular, we find $\sim 60\times - 70\times$ Nurion CPU node-hr to Frontier GPU node-hr speedups, underscoring the importance of the numerical strategies developed in this work amenable for efficient implementation on GPUs as well.

3. Scalability

We now assess the parallel scalability (strong scaling) of our numerical implementation involving noncollinear magnetism and spin-orbit coupling (NCSOC-DFT-FE) on

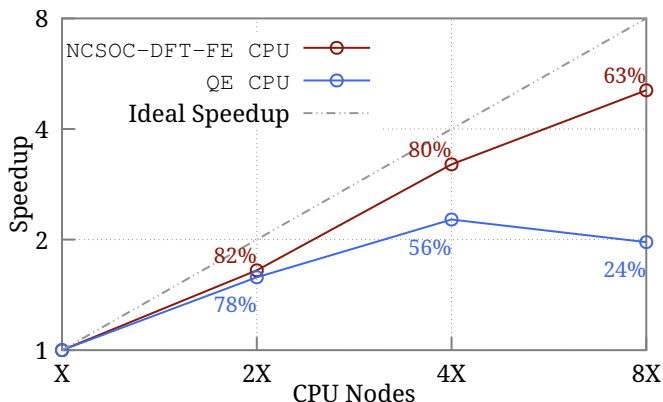


FIG. 2. Relative speed up of wall-time per SCF iteration for the 49° twist angle bilayer WTe₂ for varying number of KNL CPU nodes on Nurion. NCSOC-DFT-FE: The value of X is 100, and the total number of DoFs is 6509526. The number of band groups at X, 2X, 4X, and 8X is 1, 1, 2, and 4, respectively. QE: The value of X is 20, and the number of plane waves is 577425. Number of band groups at X, 2X, 4X, and 8X is 1, 1, 2, and 2 respectively

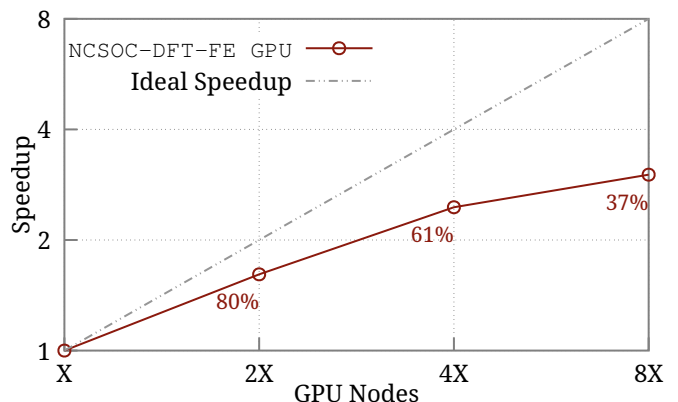


FIG. 3. Relative speed up of wall-time per SCF iteration for the 49° twist angle bilayer WTe₂ for varying number of GPU nodes on Frontier. NCSOC-DFT-FE: The value of X is 8, and the total number of DoFs is 6509526.

both multi-node CPUs and GPUs. We choose the W₁₁₆Te₂₃₂ system containing around 6.5 million degrees of freedom (number of finite-element basis functions) as our benchmark system and present the relative speed ups with respect to the minimum number of both CPU and GPU nodes the problem could fit on. Figure 2 compares the scaling behavior of NCSOC-DFT-FE with QE on KNL CPU nodes and fig. 3 demonstrates the scalability of NCSOC-DFT-FE on Frontier AMD GPUs. In both NCSOC-DFT-FE and QE, the discretization parameters are chosen such that the discretization error in the ground-state energy is $\sim \mathcal{O}(10^{-4})$ Ha/atom as in previous studies. As evident from the figure, we obtain a scaling efficiency of $\sim 63\%$ even at 800 KNL CPU nodes and obtain an efficiency of $\sim 40\%$ on 64 GPU nodes (512 GPUs). In the case of QE, we find that the relative speedups obtained by increasing the number of nodes are of a limited range and flatten off early with relative speedups dropping substantially beyond a certain number of CPU nodes compared to NCSOC-DFT-FE. Using these results, table V compares the minimum wall time per SCF obtained using NCSOC-DFT-FE with QE for the twisted bi-

layer $W_{116}Te_{232}$ considered in this study. To this end, we find that our method provides nearly $8\times$ computational gains over QE in terms of minimum wall time on multi-node CPUs and more than $30\times$ on multi-node GPUs, and these gains will increase substantially with system sizes.

Method	# of nodes	Minimum Walltime per SCF (τ^{\min})
QE Nurion CPUs	80	740
NCSOC-DFT-FE Nurion CPUs	800	99
NCSOC-DFT-FE Frontier GPUs	64	26

TABLE V. Computational cost (τ^{\min}) comparison between NCSOC-DFT-FE and QE in terms of minimum walltime (discretization error $\sim 10^{-4}$ Ha/atom). **Case Study:** 49° twist angle bilayer WTe_2

B. Periodic systems

We now discuss the case of fully periodic systems for accuracy and performance benchmarking. In particular, we benchmark the accuracy of NCSOC-DFT-FE with QE by comparing the ground-state energies, volume integral of magnetization density, magnetic anisotropy energies and the bandstructure of representative periodic systems. We further assess the performance of our implementation by comparing the computational cost of NCSOC-DFT-FE with QE by considering periodic systems involving MnSi supercells of various sizes ranging from 288 atoms (2736 electrons) to 1568 atoms (14896 electrons). In NCSOC-DFT-FE, we apply periodic boundary conditions when solving for the wavefunctions and the electrostatic potential using eqs. (39) and (63), additionally we impose the constraint that the mean electrostatic potential in a periodic unit-cell is zero to obtain a unique solution for the electrostatic potential in eq. (63). Periodic boundary conditions are used in QE for these calculations.

1. Accuracy benchmarking

In our accuracy benchmarking studies of periodic systems reported here comparing NCSOC-DFT-FE with QE, we use a kinetic energy cutoff (`ecutwfc`) of 75Ha in QE while a polynomial order of 6 with a finite-element mesh size of 0.8 Bohr is used in our method.

a. Energetics: Table (VI) shows the comparison of total internal energies with QE for the relaxed, periodic face-centred-cubic GaAs primitive unit-cell that display

spin-orbit interaction and cubic MnSi primitive unit-cell the exhibit noncollinear magnetism. In both QE and NCSOC-DFT-FE, shifted $8 \times 8 \times 8$ and $3 \times 3 \times 3$ Monkhorst-Pack k-point grids are used to sample the Brillouin zone for GaAs and MnSi unit-cells, respectively. From the table VI, we observe an excellent match between NCSOC-DFT-FE and QE. Additionally, we compare

System	QE (Ha)	NCSOC-DFT-FE (Ha)	Error (Ha/atom)
GaAs	-182.528415	-182.528306	5.5E-05
MnSi	-452.671967	-452.671811	1.9E-05

TABLE VI. Accuracy benchmarks for total internal energy.

the volume integral of the magnitude of magnetization density for the case of MnSi primitive unit-cell in table VII and observe a close match between NCSOC-DFT-FE and QE.

System	QE (Bohr Magneton)	NCSOC-DFT-FE (Bohr Magneton)	Error (Bohr Magneton)
MnSi	4.6941	4.6902	3.9E-03

TABLE VII. Accuracy benchmarks for volume integral of the magnitude of magnetization density.

b. Magneto-Crystalline Anisotropy We also benchmark the magnetocrystalline anisotropy energy for the tetragonal bulk transition metal alloy FePt, which is known to exhibit magnetocrystalline anisotropy [95, 96]. To this end, in both QE and NCSOC-DFT-FE we utilize a $16 \times 16 \times 12$ Monkhorst-Pack grid [92] and compute the energy difference for the cases with the magnetization density pointing along the z-axis (E_z) and with the magnetization density pointing along the x-axis (E_x)

System	QE (meV)	NCSOC-DFT-FE (meV)	Error (meV)
FePt	2.747	2.743	4.1E-03

TABLE VIII. Accuracy benchmarks for the magneticcrystalline anisotropy energy.

c. Band-structure: We also compute the band structure of GaAs, which is known to exhibit band-splitting due to SOC. To this end, we compute the ground-state electron density for the structures obtained from the Materials-Project database [97] using the SCF procedure with a $8 \times 8 \times 8$ Monkhorst-Pack grid [92] for Brillouin zone sampling followed by a non-SCF calculation to obtain the eigenvalues along the chosen high-symmetry path. Figure 4 shows the band structure of GaAs with and without SOC obtained from our method. We see

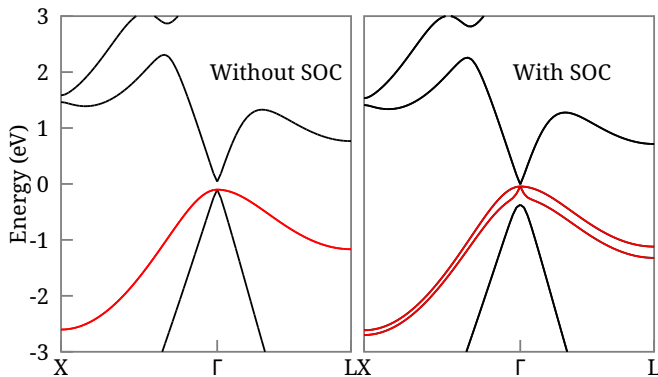


FIG. 4. Bandstructure of GaAs with and without SOC, the bands shown in red serve as an example for band splitting

that the band structure obtained from our NCSOC-DFT-FE calculations demonstrates the splitting of the heavy hole band (shown in red). At the Γ -point, we see that SOC splits the triply degenerate valence states into a doubly degenerate state and a non-degenerate state. This is consistent with existing literature [98, 99].

2. Performance studies

We now discuss the performance of NCSOC-DFT-FE with QE by comparing the average CPU time per SCF iteration in terms of computational node-hrs (η_c) with increasing system sizes of a periodic system solved to a similar level of accuracy. Particularly, we consider MnSi supercells of increasing sizes. The Skyrmion radius in MnSi is ~ 10 nm, and any computational study of Skyrmions in MnSi requires large supercells. To this end, periodic pseudopotential DFT calculations involving noncollinear magnetism and spin-orbit coupling terms are conducted on MnSi supercells of sizes $6 \times 6 \times 1$ (2736 electrons), $8 \times 8 \times 1$ (4864 electrons), $10 \times 10 \times 1$ (7600 electrons), $12 \times 12 \times 1$ (10944 electrons), and $14 \times 14 \times 1$ (14896 electrons). Table IX summarizes the configurations and number of atoms considered in increasing supercell size.

We employ the PBE functional [89] for the exchange-correlation and fully-relativistic optimized norm-conserving pseudopotentials (ONCV) [60] in the Pseudo-dojo database [90]. In order to evaluate the performance in a consistent manner, we choose the basis set parameters such that the error in the ground-state energy due to the discretization is $\sim 10^{-4}$ Ha/atom. To this end, we use a kinetic energy cutoff (`ecutwfc`) of 45Ha in QE and a polynomial order of 7 with a mesh size of 1.2 Bohr in our method. We perform a noncollinear calculation with SOC in both our method and QE using a $1 \times 1 \times 3$ Monkhorst-Pack grid [92] for Brillouin zone sampling employing periodic boundary conditions in all three directions.

Table IX shows the average CPU time per SCF iteration in terms of computational node-hrs (η_c) and

the number of basis functions in NCSOC-DFT-FE and QE for various sizes of MnSi supercells considered in this study. We find that for system sizes ~ 8000 electrons and above, NCSOC-DFT-FE becomes more efficient than QE with increasing system size on CPUs. From the above table, the computational complexity in the regime of $\sim 3000 - 15000$ electrons for NCSOC-DFT-FE is estimated to be around $\mathcal{O}(N_e^{2.3})$ while in the case of QE, it is around $\mathcal{O}(N_e^{3.3})$. The higher computational complexity of QE is attributed to the requirement of a large number of processors to meet the peak memory requirement that affects the scalability of QE. The efficient parallel scalability of our methods provides the necessary advantage in terms of computational node-hrs as the system size increases. Furthermore, table IX also reports the average time per SCF iteration in terms of GPU node-hrs (η_g), and we find $\sim 40 \times - 50 \times$ Nurion CPU node-hr to Frontier GPU node-hr speedups, highlighting the significant advantage of our computational method on GPUs.

3. Scalability

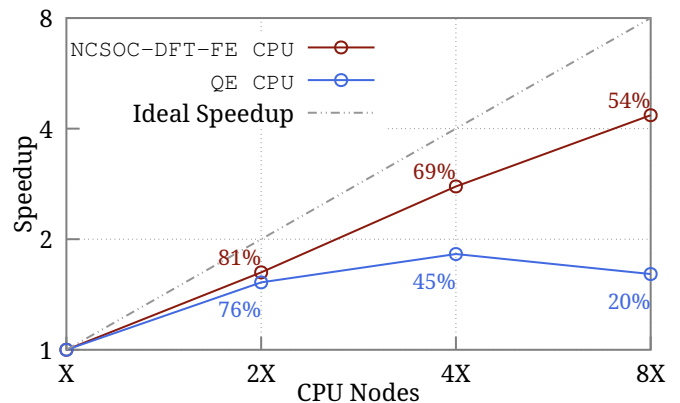


FIG. 5. Relative speed ups of wall-time per SCF iteration per k-Point for the $8 \times 8 \times 1$ supercell of MnSi with 4864 electrons for varying number of nodes on Nurion. NCSOC-DFT-FE: The value of X is 100, and the total number of DoFs is 7722450. The number of band groups at X, 2X, 4X, and 8X is 1, 1, 2, and 4, respectively. QE: The value of X is 16, and the total number of plane-waves is 574029. The number of band groups at X, 2X, 4X, and 8X is 1, 1, 2, and 2 respectively.

We now demonstrate the parallel strong scaling of our implementation in the case of periodic $8 \times 8 \times 1$ supercell on both multi-node CPUs and GPUs. The MnSi supercell considered in this study involves around 7.7 million degrees of freedom (number of grid points/FE basis functions). Figure 5 compares the scaling behavior of NCSOC-DFT-FE with QE on Nurion KNL CPU nodes and fig. 6 demonstrates the scalability of NCSOC-DFT-FE on Frontier AMD GPUs, with the lowest number of nodes chosen in each case to be the minimum number of nodes that the problem could fit on. In both approaches, the discretization parameters are chosen such that the dis-

Supercell size	Atoms	Electrons	QE # of basis fns.	QE Nurion CPU Node-hrs (η_c)	NCSOC-DFT-FE # of basis fns.	NCSOC-DFT-FE Nurion CPU Node-hrs (η_c)	NCSOC-DFT-FE Frontier GPU Node-hrs (η_g)
6x6x1	288	2736	322917	0.8	4351250	2.5	0.04
8x8x1	512	4864	574029	5.7	7722450	8.4	0.2
10x10x1	800	7600	896981	26.5	12400200	26.0	0.6
12x12x1	1152	10944	1291453	132.4	17760800	71.4	1.2
14x14x1	1568	14896	1757965	— ^a	24081800	154.4	2.8

^a We were unable to perform this computation due to memory limitations on KNL architectures

TABLE IX. Computational cost (η) comparison between NCSOC-DFT-FE and QE in node-hrs (discretization error $\sim 10^{-4}$ Ha/atom). η is computed as the product of the minimum number of nodes required to fit a given material system and the average wall time taken per SCF iteration. **Case Study:** MnSi periodic supercells

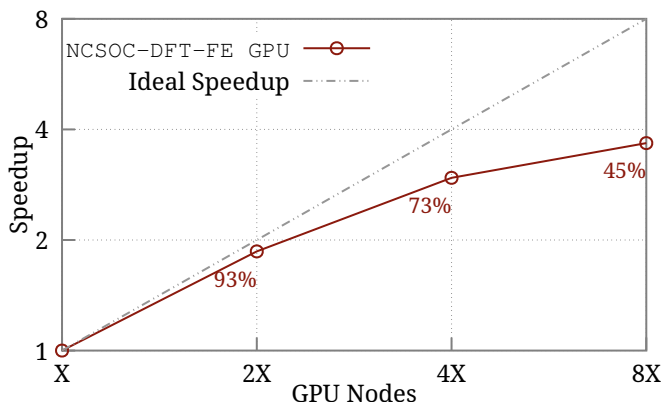


FIG. 6. Relative speed ups of wall-time per SCF iteration per k-Point for the 8x8x1 supercell of MnSi with 4864 electrons for varying number of nodes on Frontier. NCSOC-DFT-FE: The value of X is 8, and the total number of DoFs is 7722450.

cretization error in ground-state energy is $\mathcal{O}(10^{-4})$ as in previous performance studies. As evident from the figure, we observe a scaling efficiency of $\sim 54\%$ even on 800 KNL compute nodes and an efficiency of $\sim 45\%$ on 64 GPU nodes. Similar to the semi-periodic case of WTe₂,

Method	# of nodes	Minimum Walltime per SCF (τ^{\min})
QE Nurion CPUs	64	709
NCSOC-DFT-FE Nurion CPUs	800	69
NCSOC-DFT-FE Frontier GPUs	64	21

TABLE X. Computational cost (τ^{\min}) comparison between NCSOC-DFT-FE and QE in terms of minimum walltime per scf per k-point (discretization error $\sim 10^{-4}$ Ha/atom). **Case Study:** 8x8x1 supercell of MnSi

we find the relative speedups obtained in QE are of a limited range, with speedups flattening off beyond a certain number of nodes. To this end, a comparison of minimum wall times per SCF iteration per k-point between the two approaches for this medium-scale system containing 4864 electrons shows a massive $11 \times$ gains over QE on multi-node CPU nodes and more than $30 \times$ gains on multi-node GPU nodes, underscoring the excellent parallel scalability of our numerical implementation. We note that these gains will increase with an increase in system sizes.

VI. SUMMARY

In this work, we present a computationally efficient and systematically convergent real-space finite-element based methodology for large-scale pseudopotential density functional theory (DFT) calculations incorporating noncollinear magnetism and spin-orbit coupling effects. The development of the proposed approach is based on the following key ideas. First, we deduced the finite-element (FE) discretized governing equations involving 2-component spinors wherein we have made use of a local real-space formulation to evaluate the electrostatic potential. We have also devised a numerical strategy extending the ideas of the White-Bird approach to evaluate the GGA exchange-correlation potential for noncollinear magnetism within the FE framework of DFT involving C^0 basis functions. This strategy mitigated the need to deal with the gradient of the magnetization direction, whose integral is unbounded as the magnetization tends to zero. Subsequently, we developed efficient methods that exploit the sparsity of local and non-local parts of the FE discretized Hamiltonian matrix to compute the action of this matrix on a trial subspace of vectors. These methods were leveraged alongside a self-consistent field (SCF) iteration approach with the Chebyshev filtered subspace iteration procedure to solve the underlying FE discretized generalized eigenvalue problem based on a two-grid strategy. Furthermore, we introduced a unified approach to compute atomic forces and unit-cell stresses

in the presence of noncollinear magnetism and spin-orbit coupling. This approach, based on the configurational force method, evaluates the directional derivative of a generalized energy functional with the a stationary point at the minima of the Kohn-Sham functional.

We validated the accuracy of the proposed method against a plane-wave implementation of noncollinear magnetism and spin-orbit interaction across various representative benchmark systems, including non-periodic, semi-periodic, and fully periodic systems. Our proposed methodology(NCSOC-DFT-FE) showed excellent agreement with the plane-wave calculations for several key metrics, including ground-state energies, vertical ionization potentials, magnetic anisotropy energies, band structures, and spin-textures. Furthermore, compared to the state-of-the-art plane-wave implementation, the efficient computational strategies employed in NCSOC-DFT-FE enabled a $2\times$ reduction in computational cost in material systems involving 15000-20000 electrons on CPUs. Additionally, our method achieves substantial speed ups ($\sim 8\times - 11\times$) in terms of minimum wall-time compared to state-of-the-art plane-wave code (QE) for both semi-periodic and non-periodic systems. Furthermore, the proposed computational strategies exhibit excellent parallel scaling efficiency (up to $\sim 63\%$) even on 800 KNL compute nodes. We have also demonstrated the performance of our methodology on the Frontier exascale system wherein we have achieved $\sim 50x$ reduction in node-hrs compared to the KNL CPU architecture. We also achieve parallel scaling efficiency of up to $\sim 45\%$ on 64 nodes on Frontier.

The proposed work, NCSOC-DFT-FE, takes advantage of the compactly supported nature of finite-element (FE) basis functions and their adaptive resolution, enabling efficient use of modern supercomputing architectures, resulting in a substantial computational advantage over the current state-of-the-art plane-wave-based implementations for medium to large-scale material systems. Thus, the proposed methodology allows for studying non-collinear magnetism and spin-orbit coupling effects on larger length scales from first principles, significantly enhancing the scope of *ab-initio* computations for systems where such effects play a crucial role.

We note that the current implementation does not utilize the recently proposed matrix-free algorithms for ma-

trix multivector products [40], which take advantage of the tensor-structured nature of the FE basis and show great promise in further accelerating real-space FE-based density functional theory computations. Hence, as part of future work, we aim to extend the matrix-free algorithms to the two-component complex spinor framework required to incorporate noncollinear magnetism and spin-orbit coupling effects in DFT, which would further reduce the computational cost of our method. We also aim to extend our proposed methodology and incorporate noncollinear magnetism and spin-orbit coupling effects within the framework of the recently introduced finite-element based projector-augmented wave method [41] which has been shown to require considerably fewer number of basis functions when compared to the ONCV framework. Finally, we aim to utilize our proposed methodologies to solve large-scale problems of scientific interest involving SOC and noncollinear magnetism employing periodic/semi-periodic/fully non-periodic boundary conditions from an *ab-initio* perspective.

VII. ACKNOWLEDGEMENTS

The authors gratefully acknowledge the seed grant from the Indian Institute of Science and the SERB Startup Research Grant from the Department of Science and Technology India (Grant Number: SRG/2020/002194). The research used the resources of PARAM Pravega at the Indian Institute of Science, supported by the National Supercomputing Mission (NSM). The research also used resources from KIST Supercomputer Nurion in South Korea for all the CPU calculations. This research also used GPU resources from the Oak Ridge Leadership Computing Facility at the Oak Ridge National Laboratory, supported by the Office of Science of the U.S. Department of Energy under Contract No. DE-AC05-00OR22725. N.K. would like to acknowledge the Prime Minister Research Fellowship(PMRF) from the Ministry of Education India and the Council of Scientific and Industrial Research (CSIR) fellowship for financial support. P.M. acknowledges Google India Research Award 2023 and Indo-Korean Science and Technology Center Bengaluru for financial support during the course of this work

Appendix A: Stationary properties of the generalized functional

Consider the generalized functional

$$\begin{aligned} \tilde{E}[\tilde{V}, \tilde{\mathbf{B}}, \tilde{\rho}, \tilde{\mathbf{m}}, \tilde{f}_{n\mathbf{k}}] = & \sum_n \int_{BZ} \tilde{f}_{n\mathbf{k}} \epsilon_{n\mathbf{k}}[\tilde{V}, \tilde{\mathbf{B}}] d\mathbf{k} - \int (\tilde{V}\tilde{\rho} + \tilde{\mathbf{B}} \cdot \tilde{\mathbf{m}}) d\mathbf{r} + E_{\text{el}}[\tilde{\rho}, \mathbf{R}] + E_{\text{xc}}[\tilde{\rho}, \tilde{\mathbf{m}}] \\ & + E_{\text{ent}}[\tilde{f}_{n\mathbf{k}}] + \mu \left(N_e - \sum_n \int_{BZ} \tilde{f}_{n\mathbf{k}} d\mathbf{k} \right) \quad (\text{A1}) \end{aligned}$$

The functional derivatives of this functional can be written as

$$\frac{\delta \tilde{E}}{\delta \tilde{V}} = \rho[\tilde{V}, \tilde{\mathbf{B}}] - \tilde{\rho} \quad (\text{A2})$$

$$\frac{\delta \tilde{E}}{\delta \tilde{\mathbf{B}}} = \mathbf{m}[\tilde{V}, \tilde{\mathbf{B}}] - \tilde{\mathbf{m}} \quad (\text{A3})$$

$$\frac{\delta \tilde{E}}{\delta \tilde{\rho}} = V[\tilde{\rho}, \tilde{\mathbf{m}}] - \tilde{V} \quad (\text{A4})$$

$$\frac{\delta \tilde{E}}{\delta \tilde{\mathbf{m}}} = \mathbf{B}[\tilde{\rho}, \tilde{\mathbf{m}}] - \tilde{\mathbf{B}} \quad (\text{A5})$$

$$\frac{\delta \tilde{E}}{\delta \tilde{f}_{nk}} = \epsilon_{nk}[\tilde{V}, \tilde{\mathbf{B}}] - \mu + k_B T \ln \frac{\tilde{f}_{nk}}{1 - \tilde{f}_{nk}} \quad (\text{A6})$$

where we have defined $\rho[\tilde{V}, \tilde{\mathbf{B}}]$ and $\mathbf{m}[\tilde{V}, \tilde{\mathbf{B}}]$ as the total charge and magnetization densities computed using the wavefunctions obtained as solution of the eigenvalue problem defined by eq. (30) using eqs. (4) and (5). We also define $V[\tilde{\rho}, \tilde{\mathbf{m}}]$ and $\mathbf{B}[\tilde{\rho}, \tilde{\mathbf{m}}]$ as

$$V[\tilde{\rho}, \tilde{\mathbf{m}}] = V_{\text{el}}[\tilde{\rho}] + V_{\text{xc}}[\tilde{\rho}, \tilde{\mathbf{m}}] \quad (\text{A7})$$

$$\mathbf{B}[\tilde{\rho}, \tilde{\mathbf{m}}] = \mathbf{B}_{\text{xc}}[\tilde{\rho}, \tilde{\mathbf{m}}] \quad (\text{A8})$$

where $V_{\text{xc}}[\tilde{\rho}, \tilde{\mathbf{m}}]$ and $\mathbf{B}_{\text{xc}}[\tilde{\rho}, \tilde{\mathbf{m}}]$ are given by

$$V_{\text{xc}}[\tilde{\rho}, \tilde{\mathbf{m}}] = \left. \frac{\delta E_{\text{xc}}}{\delta \rho} \right|_{\substack{\rho=\tilde{\rho} \\ \mathbf{m}=\tilde{\mathbf{m}}}} \quad \mathbf{B}_{\text{xc}}[\tilde{\rho}, \tilde{\mathbf{m}}] = \left. \frac{\delta E_{\text{xc}}}{\delta \mathbf{m}} \right|_{\substack{\rho=\tilde{\rho} \\ \mathbf{m}=\tilde{\mathbf{m}}}} \quad (\text{A9})$$

and $V_{\text{el}}[\tilde{\rho}]$ is given as the solution of

$$-\nabla^2 V_{\text{el}} = 4\pi(\tilde{\rho} + b) \quad (\text{A10})$$

Setting the functional derivatives in eqs. (A2) to (A6) to zero and after straightforward algebraic manipulations we obtain

$$\rho[V[\tilde{\rho}, \tilde{\mathbf{m}}], \mathbf{B}[\tilde{\rho}, \tilde{\mathbf{m}}]] = \tilde{\rho} \quad (\text{A11})$$

$$\mathbf{m}[V[\tilde{\rho}, \tilde{\mathbf{m}}], \mathbf{B}[\tilde{\rho}, \tilde{\mathbf{m}}]] = \tilde{\mathbf{m}} \quad (\text{A12})$$

Or equivalently

$$F[(\tilde{\rho}, \tilde{\mathbf{m}})] = (\tilde{\rho}, \tilde{\mathbf{m}}) \quad (\text{A13})$$

which is the solution to the Kohn-Sham eigenproblem defined by eqs. (25) and (26). Thus we can conclude that the generalized functional defined in eq. (29) has a stationary point at the solution to the Kohn-Sham eigenvalue problem.

Appendix B: Gateaux derivatives of the generalized functional

In order to compute the configurational force on a system due to a perturbation τ^ε we need to evaluate

$$\left. \frac{d\tilde{E}_S^\varepsilon}{d\varepsilon} \right|_{\varepsilon=0} \quad (\text{B1})$$

To this end we first write the parametrized functional \tilde{E}_S^ε in the perturbed space as

$$\begin{aligned} \tilde{E}_S^\varepsilon[V^\varepsilon, \mathbf{B}^\varepsilon, \rho^\varepsilon, \mathbf{m}^\varepsilon, f_{nk^\varepsilon}^\varepsilon] &= \sum_n \int_{BZ^\varepsilon} f_{nk^\varepsilon}^\varepsilon \epsilon_{nk^\varepsilon}^\varepsilon [V^\varepsilon, \mathbf{B}^\varepsilon] dk^\varepsilon - \int (V^\varepsilon \rho^\varepsilon + \mathbf{B}^\varepsilon \cdot \mathbf{m}^\varepsilon) d\mathbf{r}^\varepsilon + E_{\text{el}}^\varepsilon[\rho^\varepsilon, \mathbf{R}^\varepsilon] + E_{\text{xc}}^\varepsilon[\rho^\varepsilon, \mathbf{m}^\varepsilon] \\ &\quad + E_{\text{ent}}^\varepsilon[f_{nk^\varepsilon}^\varepsilon] + \mu \left(N_e - \sum_n \int_{BZ^\varepsilon} f_{nk^\varepsilon}^\varepsilon dk^\varepsilon \right) \end{aligned} \quad (\text{B2})$$

where V^ε , \mathbf{B}^ε , ρ^ε , \mathbf{m}^ε and f_{nk}^ε represent the solutions of the stationary point in the perturbed space and consequently they satisfy the Euler-lagrange equations obtained by setting eqs. (A2) to (A6) to zero. Note that $\boldsymbol{\tau}^{\varepsilon=0} = \mathbb{I}$ and consequently we drop the superscript of ε when $\varepsilon = 0$ for notational convenience. The derivative can now be written as

$$\begin{aligned} \left. \frac{d\tilde{E}_S^\varepsilon[V^\varepsilon, \mathbf{B}^\varepsilon, \rho^\varepsilon, \mathbf{m}^\varepsilon, f_{nk}^\varepsilon]}{d\varepsilon} \right|_{\varepsilon=0} &= \left. \frac{\partial \tilde{E}_S^\varepsilon[V, \mathbf{B}, \rho, \mathbf{m}, f_{nk}]}{\partial \varepsilon} \right|_{\varepsilon=0} + \int d\mathbf{r}^\varepsilon \left. \frac{\delta \tilde{E}_S^\varepsilon}{\delta \rho^\varepsilon(\mathbf{r}^\varepsilon)} \frac{d\rho^\varepsilon(\mathbf{r}^\varepsilon)}{d\varepsilon} \right|_{\varepsilon=0} + \int d\mathbf{r}^\varepsilon \left. \frac{\delta \tilde{E}_S^\varepsilon}{\delta \mathbf{m}^\varepsilon(\mathbf{r}^\varepsilon)} \cdot \frac{d\mathbf{m}^\varepsilon(\mathbf{r}^\varepsilon)}{d\varepsilon} \right|_{\varepsilon=0} \\ &+ \int d\mathbf{r}^\varepsilon \left. \frac{\delta \tilde{E}_S^\varepsilon}{\delta V^\varepsilon(\mathbf{r}^\varepsilon)} \frac{dV^\varepsilon(\mathbf{r}^\varepsilon)}{d\varepsilon} \right|_{\varepsilon=0} + \int d\mathbf{r}^\varepsilon \left. \frac{\delta \tilde{E}_S^\varepsilon}{\delta \mathbf{B}^\varepsilon(\mathbf{r}^\varepsilon)} \cdot \frac{d\mathbf{B}^\varepsilon(\mathbf{r}^\varepsilon)}{d\varepsilon} \right|_{\varepsilon=0} + \int_{BZ} d\mathbf{k}^\varepsilon \left. \frac{\delta \tilde{E}_S^\varepsilon}{\delta f_{nk}^\varepsilon} \frac{df_{nk}^\varepsilon}{d\varepsilon} \right|_{\varepsilon=0} \end{aligned} \quad (\text{B3})$$

we note that at the stationary point, all the functional derivatives (eqs. (A2) to (A6)) are zero, consequently we can write

$$\left. \frac{d\tilde{E}_S^\varepsilon[V^\varepsilon, \mathbf{B}^\varepsilon, \rho^\varepsilon, \mathbf{m}^\varepsilon, f_{nk}^\varepsilon]}{d\varepsilon} \right|_{\varepsilon=0} = \left. \frac{\partial \tilde{E}_S^\varepsilon[V, \mathbf{B}, \rho, \mathbf{m}, f_{nk}]}{\partial \varepsilon} \right|_{\varepsilon=0} \quad (\text{B4})$$

where $\tilde{E}_S^\varepsilon[V, \mathbf{B}, \rho, \mathbf{m}, f_{nk}]$ can be written as

$$\begin{aligned} \tilde{E}_S^\varepsilon[V, \mathbf{B}, \rho, \mathbf{m}, f_{nk}] &= \sum_n \int_{BZ^\varepsilon} f_{nk} \epsilon_{nk}^\varepsilon [V, \mathbf{B}] d\mathbf{k}^\varepsilon - \int (V\rho + \mathbf{B} \cdot \mathbf{m}) d\mathbf{r}^\varepsilon + E_{\text{el}}^\varepsilon[\rho, \mathbf{R}^\varepsilon] + E_{\text{xc}}^\varepsilon[\rho, \mathbf{m}] \\ &+ E_{\text{ent}}^\varepsilon[f_{nk}] + \mu \left(N_e - \sum_n \int_{BZ^\varepsilon} f_{nk} d\mathbf{k}^\varepsilon \right) \end{aligned} \quad (\text{B5})$$

We can now transform the integrals in the above equation into integrals over the unperturbed space, allowing us to write

$$\begin{aligned} \tilde{E}_S^\varepsilon &= \sum_n \int_{BZ} f_{nk} \epsilon_{nk}^\varepsilon [V, \mathbf{B}] d\mathbf{k} - \int (V\rho + \mathbf{B} \cdot \mathbf{m}) \det \left(\frac{\partial \mathbf{r}^\varepsilon}{\partial \mathbf{r}} \right) d\mathbf{r} + E_{\text{el}}^\varepsilon[\rho, \mathbf{R}^\varepsilon] + E_{\text{xc}}^\varepsilon[\rho, \mathbf{m}] \\ &+ E_{\text{ent}}^\varepsilon[f_{nk}] + \mu \left(N_e - \sum_n \int_{BZ} f_{nk} d\mathbf{k} \right) \end{aligned} \quad (\text{B6})$$

The required partial derivative can now be written as

$$\begin{aligned} \left. \frac{\partial \tilde{E}_S^\varepsilon}{\partial \varepsilon} \right|_{\varepsilon=0} &= \sum_n \int_{BZ} d\mathbf{k} f_{nk} \left. \frac{\partial \epsilon_{nk}^\varepsilon [V, \mathbf{B}]}{\partial \varepsilon} \right|_{\varepsilon=0} - \int d\mathbf{r} (V\rho + \mathbf{B} \cdot \mathbf{m}) \left. \frac{\partial}{\partial \varepsilon} \left\{ \det \left(\frac{\partial \mathbf{r}^\varepsilon}{\partial \mathbf{r}} \right) \right\} \right|_{\varepsilon=0} + \left. \frac{\partial E_{\text{el}}^\varepsilon[\rho, \mathbf{R}^\varepsilon]}{\partial \varepsilon} \right|_{\varepsilon=0} \\ &+ \left. \frac{\partial E_{\text{xc}}^\varepsilon[\rho, \mathbf{m}]}{\partial \varepsilon} \right|_{\varepsilon=0} \end{aligned} \quad (\text{B7})$$

For the evaluation of the partial derivative of the term corresponding to the total electrostatic energy we refer to [39, 50]. We now discuss the evaluation of the rest of the terms.

1. Gateaux derivative of the eigenvalue

Consider the first term in eq. (B7), we need to evaluate the derivative of the eigenvalues in the perturbed space

$$\left. \frac{\partial \epsilon_{nk}^\varepsilon [V, \mathbf{B}]}{\partial \varepsilon} \right|_{\varepsilon=0} = \left. \frac{\partial \langle \mathbf{u}_{nk}^\varepsilon | \mathcal{H}_\varepsilon^{k^\varepsilon} [V, \mathbf{B}] | \mathbf{u}_{nk}^\varepsilon \rangle_\varepsilon}{\partial \varepsilon} \right|_{\varepsilon=0} \quad (\text{B8})$$

We can now invoke the Hellmann–Feynman theorem

$$\left. \frac{\partial \epsilon_{nk}^\varepsilon [V, \mathbf{B}]}{\partial \varepsilon} \right|_{\varepsilon=0} = \langle \mathbf{u}_{nk}^\varepsilon | \left. \frac{\partial \mathcal{H}_\varepsilon^{k^\varepsilon} [V, \mathbf{B}]}{\partial \varepsilon} \right|_{\varepsilon=0} | \mathbf{u}_{nk}^\varepsilon \rangle_\varepsilon \quad (\text{B9})$$

We can now write

$$\left. \frac{\partial \mathcal{H}_\varepsilon^{k^\varepsilon} [V, \mathbf{B}]}{\partial \varepsilon} \right|_{\varepsilon=0} = \left. \frac{\partial \mathcal{H}_\varepsilon^{k^\varepsilon, \text{loc}} [V, \mathbf{B}]}{\partial \varepsilon} \right|_{\varepsilon=0} + \left. \frac{\partial \mathcal{H}_\varepsilon^{k^\varepsilon, \text{nloc}}}{\partial \varepsilon} \right|_{\varepsilon=0} \quad (\text{B10})$$

Consequently for the local part of the Hamiltonian we can write

$$\langle \mathbf{u}_{n\mathbf{k}} | \frac{\partial \mathcal{H}_\varepsilon^{\mathbf{k}^\varepsilon, \text{loc}}[V, \mathbf{B}]}{\partial \varepsilon} |_{\varepsilon=0} | \mathbf{u}_{n\mathbf{k}} \rangle = \frac{\partial}{\partial \varepsilon} \left\{ \int \left(-\frac{\mathbf{u}_{n\mathbf{k}}^\dagger \nabla_\varepsilon^2 \mathbf{u}_{n\mathbf{k}}}{2} - \mathbf{u}_{n\mathbf{k}}^\dagger i\mathbf{k}^\varepsilon \cdot \nabla_\varepsilon \mathbf{u}_{n\mathbf{k}} + \frac{|\mathbf{k}^\varepsilon|^2}{2} \mathbf{u}_{n\mathbf{k}}^\dagger \mathbf{u}_{n\mathbf{k}} + (V + V_{\text{loc}}^\varepsilon - V_{\text{self}}^\varepsilon) \mathbf{u}_{n\mathbf{k}}^\dagger \mathbf{u}_{n\mathbf{k}} + \mathbf{u}_{n\mathbf{k}}^\dagger \mathbf{B} \cdot \boldsymbol{\sigma} \mathbf{u}_{n\mathbf{k}} \right) d\mathbf{r} \right\} \Big|_{\varepsilon=0} \quad (\text{B11})$$

Upon further simplification, this results in

$$\begin{aligned} \langle \mathbf{u}_{n\mathbf{k}} | \frac{\partial \mathcal{H}_\varepsilon^{\mathbf{k}^\varepsilon, \text{loc}}[V, \mathbf{B}]}{\partial \varepsilon} | \mathbf{u}_{n\mathbf{k}} \rangle &= \int \left(\frac{1}{2} \left(\nabla \mathbf{u}_{n\mathbf{k}}^\dagger \otimes \nabla \mathbf{u}_{n\mathbf{k}} + \nabla \mathbf{u}_{n\mathbf{k}} \otimes \nabla \mathbf{u}_{n\mathbf{k}}^\dagger - i\mathbf{u}_{n\mathbf{k}}^\dagger \nabla \mathbf{u}_{n\mathbf{k}} \otimes \mathbf{k} \right) : \frac{\partial}{\partial \varepsilon} \left\{ \frac{\partial \mathbf{r}}{\partial \mathbf{r}^\varepsilon} \right\} \right. \\ &\quad \left. + \frac{1}{2} \left(\nabla \mathbf{u}_{n\mathbf{k}}^\dagger \cdot \nabla \mathbf{u}_{n\mathbf{k}} + \mathbf{u}_{n\mathbf{k}}^\dagger \nabla^2 \mathbf{u}_{n\mathbf{k}} \right) \frac{\partial}{\partial \varepsilon} \left\{ \det \frac{\partial \mathbf{r}^\varepsilon}{\partial \mathbf{r}} \right\} \right. \\ &\quad \left. - i\mathbf{u}_{n\mathbf{k}}^\dagger \frac{\partial \mathbf{k}^\varepsilon}{\partial \varepsilon} \cdot \nabla \mathbf{u}_{n\mathbf{k}} + \frac{1}{2} \frac{\partial}{\partial \varepsilon} \{ |\mathbf{k}^\varepsilon|^2 \} \mathbf{u}_{n\mathbf{k}}^\dagger \mathbf{u}_{n\mathbf{k}} + \frac{\partial V_{\text{loc}}^\varepsilon}{\partial \varepsilon} \mathbf{u}_{n\mathbf{k}}^\dagger \mathbf{u}_{n\mathbf{k}} - \frac{\partial V_{\text{self}}^\varepsilon}{\partial \varepsilon} \mathbf{u}_{n\mathbf{k}}^\dagger \mathbf{u}_{n\mathbf{k}} \right) d\mathbf{r} \quad (\text{B12}) \end{aligned}$$

In a similiar manner, for the non-local part we can write

$$\begin{aligned} \langle \mathbf{u}_{n\mathbf{k}} | \frac{\partial \mathcal{H}_\varepsilon^{\mathbf{k}^\varepsilon, \text{nloc}}[V, \mathbf{B}]}{\partial \varepsilon} |_{\varepsilon=0} | \mathbf{u}_{n\mathbf{k}} \rangle &= \sum_{a \in \Omega_p} \sum_{\chi \chi'} \sum_q \frac{\partial}{\partial \varepsilon} \int_{\Omega_p} \left(\mathbf{u}_{n\mathbf{k}}^\dagger(\mathbf{r}) e^{-i\mathbf{k}^\varepsilon \cdot (\mathbf{r}^\varepsilon - \mathbf{L}_q^\varepsilon)} p_{\chi}^a(\mathbf{r}^\varepsilon - \mathbf{L}_q^\varepsilon - \mathbf{R}_a^\varepsilon) \right) d\mathbf{r} \\ &\quad \mathbf{D}^{\gamma_a, \chi, \chi'} \int_{\Omega_p} \left(\sum_{q'} e^{i\mathbf{k}^\varepsilon \cdot (\mathbf{r}'^\varepsilon - \mathbf{L}_{q'}^\varepsilon)} p_{\chi'}^a(\mathbf{r}'^\varepsilon - \mathbf{L}_{q'}^\varepsilon - \mathbf{R}_a^\varepsilon) \mathbf{u}_{n\mathbf{k}}(\mathbf{r}') \right) \det \frac{\partial \mathbf{r}'^\varepsilon}{\partial \mathbf{r}'} d\mathbf{r}' \quad (\text{B13}) \end{aligned}$$

We now note the following relations

$$\frac{\partial}{\partial \varepsilon} \left\{ \det \frac{\partial \mathbf{r}^\varepsilon}{\partial \mathbf{r}} \right\} \Big|_{\varepsilon=0} = \mathbf{I} : \nabla \boldsymbol{\Upsilon} \quad (\text{B14})$$

$$\frac{\partial}{\partial \varepsilon} \left\{ \frac{\partial \mathbf{r}}{\partial \mathbf{r}^\varepsilon} \right\} \Big|_{\varepsilon=0} = -\nabla \boldsymbol{\Upsilon} \quad (\text{B15})$$

We also note that the Laplacian of the wavefunctions can be written as

$$\frac{1}{2} \nabla^2 u_{n\mathbf{k}} = \left(\frac{|\mathbf{k}|^2}{2} - i\mathbf{k} \cdot \nabla + V_{\text{loc}} - V_{\text{self}} + V + \mathbf{B} \cdot \boldsymbol{\sigma} + \mathcal{H}^{\mathbf{k}, \text{nloc}} - \epsilon_{n\mathbf{k}} \right) u_{n\mathbf{k}} \quad (\text{B16})$$

Combining eqs. (B12) and (B13) and using the above relations, we have

$$\sum_n \int_{BZ} d\mathbf{k} f_{n\mathbf{k}} \frac{\partial \epsilon_{n\mathbf{k}}^\varepsilon[V, \mathbf{B}]}{\partial \varepsilon} \Big|_{\varepsilon=0} = \int_{\Omega_p} \mathbf{E}_1 : \nabla \boldsymbol{\Upsilon} d\mathbf{r} + F^{\text{psp}, \text{nloc}} + F^K + F^{\text{ext}, \text{corr}} \quad (\text{B17})$$

where \mathbf{E}_1 is given by

$$\begin{aligned} \mathbf{E}_1 &= \left(\sum_n \int_{BZ} \frac{f_{n\mathbf{k}}}{2} \left(\nabla \mathbf{u}_{n\mathbf{k}}^\dagger \cdot \nabla \mathbf{u}_{n\mathbf{k}} + (|\mathbf{k}|^2 - \epsilon_{n\mathbf{k}}) \mathbf{u}_{n\mathbf{k}}^\dagger \mathbf{u}_{n\mathbf{k}} - i\mathbf{u}_{n\mathbf{k}}^\dagger \mathbf{k} \cdot \nabla \mathbf{u}_{n\mathbf{k}} \right) d\mathbf{k} + (V_{\text{loc}} - V_{\text{self}}) \rho + V \rho + \mathbf{B} \cdot \mathbf{m} \right) \mathbf{I} \\ &\quad - \sum_n \int_{BZ} \frac{f_{n\mathbf{k}}}{2} \left(\nabla \mathbf{u}_{n\mathbf{k}}^\dagger \otimes \nabla \mathbf{u}_{n\mathbf{k}} + \nabla \mathbf{u}_{n\mathbf{k}} \otimes \nabla \mathbf{u}_{n\mathbf{k}}^\dagger - i\mathbf{u}_{n\mathbf{k}}^\dagger \nabla \mathbf{u}_{n\mathbf{k}} \otimes \mathbf{k} \right) d\mathbf{k} \quad (\text{B18}) \end{aligned}$$

The term $F^{\text{psp}, \text{nloc}}$ is given by $F^{\text{psp}, \text{nloc}} = F_{\text{nloc}}^\dagger + F_{\text{nloc}}$ where F_{nloc} is given by

$$\begin{aligned} F_{\text{nloc}} &= \sum_{a \in \Omega_p} \sum_{\chi \chi'} \sum_q \sum_n \int_{BZ} \left[\int_{\Omega_p} \left(\mathbf{u}_{n\mathbf{k}}^\dagger(\mathbf{r}) e^{-i\mathbf{k} \cdot (\mathbf{r} - \mathbf{L}_q)} p_{\chi}^a(\mathbf{r} - \mathbf{L}_q - \mathbf{R}_a) \right) d\mathbf{r} \mathbf{D}^{\gamma_a, \chi, \chi'} \int_{\Omega_p} \left(\sum_{q'} e^{i\mathbf{k} \cdot (\mathbf{r}' - \mathbf{L}_{q'})} \right. \right. \\ &\quad \left. \left. p_{\chi'}^a(\mathbf{r}' - \mathbf{L}_{q'} - \mathbf{R}_a) \left(-(\boldsymbol{\Upsilon}(\mathbf{r}') - \boldsymbol{\Upsilon}(\mathbf{R}_a + \mathbf{L}_{q'})) \cdot \nabla \mathbf{u}_{n\mathbf{k}}(\mathbf{r}') - i\mathbf{k} \cdot \boldsymbol{\Upsilon}(\mathbf{R}_a) \mathbf{u}_{n\mathbf{k}}(\mathbf{r}') \right) \right) d\mathbf{r}' \right] d\mathbf{k} \quad (\text{B19}) \end{aligned}$$

The term F^K is given by

$$\begin{aligned}
F^K = & \sum_n \int_{BZ} \int_{\Omega_p} \left[-i \mathbf{u}_{n\mathbf{k}}^\dagger \frac{\partial \mathbf{k}^\varepsilon}{\partial \varepsilon} \Big|_{\varepsilon=0} \cdot \nabla \mathbf{u}_{n\mathbf{k}} + \frac{1}{2} \frac{\partial}{\partial \varepsilon} \{ |\mathbf{k}^\varepsilon|^2 \} \Big|_{\varepsilon=0} \mathbf{u}_{n\mathbf{k}}^\dagger \mathbf{u}_{n\mathbf{k}} \right] d\mathbf{r} d\mathbf{k} \\
& + \sum_{a \in \Omega_p} \sum_{\chi \chi'} \sum_q \sum_n \frac{\partial}{\partial \varepsilon} \left\{ \int_{BZ} \left[\int_{\Omega_p} \left(\mathbf{u}_{n\mathbf{k}}^\dagger(\mathbf{r}) e^{-i\mathbf{k}^\varepsilon \cdot (\mathbf{r} - \mathbf{L}_q)} p_{\chi}^a(\mathbf{r} - \mathbf{L}_q - \mathbf{R}_a) \right) d\mathbf{r} \right. \right. \\
& \left. \left. \mathbf{D}^{\gamma a, \chi, \chi'} \int_{\Omega_p} \left(\sum_{q'} e^{i\mathbf{k}^\varepsilon \cdot (\mathbf{r}' - \mathbf{L}_{q'})} p_{\chi'}^a(\mathbf{r}' - \mathbf{L}_{q'} - \mathbf{R}_a) \mathbf{u}_{n\mathbf{k}}(\mathbf{r}') \right) d\mathbf{r}' \right] d\mathbf{k} \right\} \Big|_{\varepsilon=0} \quad (B20)
\end{aligned}$$

Finally, the $F^{\text{ext,corr}}$ term is given by

$$\begin{aligned}
F^{\text{ext,corr}} = & \sum_{a \in \Omega_p} \sum_q \int_{\Omega_p} \rho \left(\nabla V_{\text{loc}}^a(\mathbf{r} - \mathbf{R}_a - \mathbf{L}_q) \cdot (\boldsymbol{\Upsilon}(\mathbf{r}) - \boldsymbol{\Upsilon}(\mathbf{R}_a + \mathbf{L}_q)) - \nabla V_{\text{self}}^a(\mathbf{r}, \mathbf{R}_a + \mathbf{L}_q) \cdot \boldsymbol{\Upsilon}(\mathbf{r}) \right. \\
& \left. - \frac{\partial V_{\text{self}}^a(\mathbf{r}, b^a(\mathbf{r}^\varepsilon - \mathbf{R}_a^\varepsilon - \mathbf{L}_q^\varepsilon))}{\partial \varepsilon} \Big|_{\varepsilon=0} \right) d\mathbf{r} \quad (B21)
\end{aligned}$$

2. Gateaux derivative of the electrostatic energy

In order to compute the Gateaux derivative of the total electrostatic energy, we follow the methodology prescribed in prior works [39, 50, 62] and define the total electrostatic energy functional ($\tilde{E}_{\text{el}}[\tilde{V}_{\text{el}}, \{\tilde{V}_{\text{self}}^a\}_{a=1}^{N_a}; \rho, \mathbf{R}]$) as

$$\begin{aligned}
E_{\text{el}}[\rho, \mathbf{R}] = & \min_{\tilde{V}_{\text{self}}^a \in H^1(\mathbb{R}^3)} \max_{\tilde{V}_{\text{el}} \in H_{\text{per}}^1(\Omega_p)} \tilde{E}_{\text{el}}[\tilde{V}_{\text{el}}, \{\tilde{V}_{\text{self}}^a\}_{a=1}^{N_a}; \rho, \mathbf{R}] = \max_{\tilde{V}_{\text{el}} \in H_{\text{per}}^1(\Omega_p)} \left\{ \int_{\Omega_p} \left[-\frac{1}{8\pi} |\nabla \tilde{V}_{\text{el}}|^2 + (\rho + b(\mathbf{r}, \mathbf{R})) \tilde{V}_{\text{el}} \right] d\mathbf{r} \right\} \\
& - \sum_{a \in \Omega_p} \max_{\tilde{V}_{\text{self}}^a \in H^1(\mathbb{R}^3)} \left\{ \int_{\mathbb{R}^3} \left[-\frac{1}{8\pi} |\nabla \tilde{V}_{\text{self}}^a|^2 + b^a(\mathbf{r} - \mathbf{R}_a) \tilde{V}_{\text{self}}^a \right] d\mathbf{r} \right\} \quad (B22)
\end{aligned}$$

Consequently in the perturbed space we can write

$$\begin{aligned}
\tilde{E}_{\text{el}}^\varepsilon[\tilde{V}_{\text{el}}^\varepsilon, \{\tilde{V}_{\text{self}}^{a^\varepsilon}\}_{a=1}^{N_a}; \rho, \mathbf{R}] = & \int_{\Omega_p^\varepsilon} \left[-\frac{1}{8\pi} |\nabla_\varepsilon \tilde{V}_{\text{el}}^\varepsilon|^2 + (\rho + b(\mathbf{r}^\varepsilon, \mathbf{R}^\varepsilon)) \tilde{V}_{\text{el}}^\varepsilon \right] d\mathbf{r}^\varepsilon - \int_{\mathbb{R}^3} \left[-\frac{1}{8\pi} |\nabla_\varepsilon \tilde{V}_{\text{self}}^{a^\varepsilon}|^2 + b^a(\mathbf{r}^\varepsilon - \mathbf{R}_a^\varepsilon) \tilde{V}_{\text{self}}^{a^\varepsilon} \right] d\mathbf{r}^\varepsilon \quad (B23)
\end{aligned}$$

We now define $V_{\text{el}}^\varepsilon$ and $V_{\text{self}}^{a^\varepsilon}$ as the solutions of the above saddle-point problem in the perturbed space. This allows us to write the Gateaux derivative of the total electrostatic energy as

$$\frac{\partial E_{\text{el}}^\varepsilon[\rho, \mathbf{R}^\varepsilon]}{\partial \varepsilon} \Big|_{\varepsilon=0} = \frac{\partial E_{\text{el}}^\varepsilon[V_{\text{el}}, \{V_{\text{self}}^a\}_{a=1}^{N_a}; \rho, \mathbf{R}]}{\partial \varepsilon} \Big|_{\varepsilon=0} + \int d\mathbf{r}^\varepsilon \frac{\delta \tilde{E}_{\text{el}}^\varepsilon}{\delta V_{\text{el}}^\varepsilon} \frac{dV_{\text{el}}^\varepsilon}{d\varepsilon} \Big|_{\varepsilon=0} + \int d\mathbf{r}^\varepsilon \frac{\delta \tilde{E}_{\text{el}}^\varepsilon}{\delta V_{\text{self}}^{a^\varepsilon}} \frac{dV_{\text{self}}^{a^\varepsilon}}{d\varepsilon} \Big|_{\varepsilon=0} \quad (B24)$$

We note that at the solution of the saddle-point problem the functional derivatives vanish, consequently we have

$$\frac{\partial E_{\text{el}}^\varepsilon[\rho, \mathbf{R}^\varepsilon]}{\partial \varepsilon} \Big|_{\varepsilon=0} = \frac{\partial E_{\text{el}}^\varepsilon[V_{\text{el}}, \{V_{\text{self}}^a\}_{a=1}^{N_a}; \rho, \mathbf{R}]}{\partial \varepsilon} \Big|_{\varepsilon=0} \quad (B25)$$

Thus we have

$$\begin{aligned}
\frac{\partial E_{\text{el}}^\varepsilon[\rho, \mathbf{R}^\varepsilon]}{\partial \varepsilon} \Big|_{\varepsilon=0} = & \frac{\partial}{\partial \varepsilon} \left\{ \int_{\Omega_p} \left[-\frac{1}{8\pi} |\nabla_\varepsilon \tilde{V}_{\text{el}}|^2 + (\rho + b(\mathbf{r}^\varepsilon, \mathbf{R}^\varepsilon)) \tilde{V}_{\text{el}} \right] \det \frac{\partial \mathbf{r}^\varepsilon}{\partial \mathbf{r}} d\mathbf{r} \right. \\
& \left. - \int_{\mathbb{R}^3} \left[-\frac{1}{8\pi} |\nabla_\varepsilon \tilde{V}_{\text{self}}^a|^2 + b^a(\mathbf{r}^\varepsilon - \mathbf{R}_a^\varepsilon) \tilde{V}_{\text{self}}^a \right] \det \frac{\partial \mathbf{r}^\varepsilon}{\partial \mathbf{r}} d\mathbf{r} \right\} \quad (B26)
\end{aligned}$$

Finally we can write

$$\left. \frac{\partial E_{\text{el}}^\varepsilon[\rho, \mathbf{R}^\varepsilon]}{\partial \varepsilon} \right|_{\varepsilon=0} = \int_{\Omega_p} \mathbf{E}_2 : \nabla \boldsymbol{\Upsilon} d\mathbf{r} + \sum_{a \in \Omega_p} \int_{\mathbb{R}^3} \mathbf{E}^a : \nabla \boldsymbol{\Upsilon} d\mathbf{r} + \mathbf{F}^{\text{sm}} \quad (\text{B27})$$

where \mathbf{E}_2 and \mathbf{E}^a are given by

$$\mathbf{E}_2 = \left(-\frac{1}{8\pi} |\nabla V_{\text{el}}|^2 + \rho V_{\text{el}} \right) \mathbf{I} + \frac{1}{4\pi} \nabla V_{\text{el}} \otimes \nabla V_{\text{el}} \quad (\text{B28})$$

$$\mathbf{E}^a = \frac{1}{8\pi} |\nabla V_{\text{self}}^a|^2 \mathbf{I} - \frac{1}{4\pi} \nabla V_{\text{self}}^a \otimes \nabla V_{\text{self}}^a \quad (\text{B29})$$

The term \mathbf{F}^{sm} is given by

$$\mathbf{F}^{\text{sm}} = \sum_{a \in \Omega_p} \sum_q \int_{\Omega_p} b^a(\mathbf{r} - \mathbf{R}_a - \mathbf{L}_q) \nabla V_{\text{el}} \cdot (\boldsymbol{\Upsilon}(\mathbf{r}) - \boldsymbol{\Upsilon}(\mathbf{R}_a + \mathbf{L}_q)) d\mathbf{r} - \sum_{a \in \Omega_p} \int_{\mathbb{R}^3} b^a(\mathbf{r} - \mathbf{R}_a) \nabla V_{\text{self}}^a \cdot (\boldsymbol{\Upsilon}(\mathbf{r}) - \boldsymbol{\Upsilon}(\mathbf{R}_a)) d\mathbf{r} \quad (\text{B30})$$

3. Gateaux derivative of the exchange-correlation energy

We now compute the Gateaux derivative of the exchange-correlation term

$$\left. \frac{\partial E_{\text{xc}}^\varepsilon[\rho, \mathbf{m}]}{\partial \varepsilon} \right|_{\varepsilon=0} = \frac{\partial}{\partial \varepsilon} \left\{ \int_{\Omega_p} f_{\text{xc}}(\rho, \mathbf{m}, \nabla_\varepsilon \rho, \nabla_\varepsilon \mathbf{m}) \det \frac{\partial \mathbf{r}^\varepsilon}{\partial \mathbf{r}} d\mathbf{r} \right\} \Big|_{\varepsilon=0} \quad (\text{B31})$$

this results in

$$\left. \frac{\partial E_{\text{xc}}^\varepsilon[\rho, \mathbf{m}]}{\partial \varepsilon} \right|_{\varepsilon=0} = \int_{\Omega_p} \mathbf{E}_3 : \nabla \boldsymbol{\Upsilon} d\mathbf{r} \quad (\text{B32})$$

where \mathbf{E}_3 is given by

$$\mathbf{E}_3 = f_{\text{xc}}(\rho, \mathbf{m}, \nabla \rho, \nabla \mathbf{m}) \mathbf{I} - \frac{\partial f_{\text{xc}}}{\partial \nabla \rho} \otimes \nabla \rho - \frac{\partial f_{\text{xc}}}{\partial \nabla |\mathbf{m}|} \otimes \nabla |\mathbf{m}| \quad (\text{B33})$$

The total configurational force is now given by

$$\left. \frac{d\tilde{E}_S^\varepsilon}{d\varepsilon} \right|_{\varepsilon=0} = \int_{\Omega_p} \mathbf{E} : \nabla \boldsymbol{\Upsilon} d\mathbf{r} + \sum_{a \in \Omega_p} \int_{\mathbb{R}^3} \mathbf{E}^a : \nabla \boldsymbol{\Upsilon} d\mathbf{r} + \mathbf{F}^{\text{psp,nloc}} + \mathbf{F}^{\mathcal{K}} + \mathbf{F}^{\text{ext,corr}} + \mathbf{F}^{\text{sm}} \quad (\text{B34})$$

Where \mathbf{E} is given by $\mathbf{E} = \mathbf{E}_1 + \mathbf{E}_2 + \mathbf{E}_3 - \rho V - \mathbf{B} \cdot \mathbf{m}$

-
- [1] L. Kleinman, Physical Review B **21**, 2630 (1980).
[2] G. Theurich and N. A. Hill, Physical Review B **64**, 073106 (2001).
[3] I. Chatratin, B. Dou, S.-H. Wei, and A. Janotti, The Journal of Physical Chemistry Letters **14**, 273 (2023).
[4] H. C. Choi, S.-Z. Lin, and J.-X. Zhu, Physical Review B **93**, 115112 (2016).
[5] Z. He and H. Weng, npj Quantum Materials **6**, 101 (2021).
[6] L. Kronik, A. Makmal, M. L. Tiago, M. M. G. Alemany,

- M. Jain, X. Huang, Y. Saad, and J. R. Chelikowsky, physica status solidi (b) **243**, 1063 (2006).
[7] V. Michaud-Rioux, L. Zhang, and H. Guo, Journal of Computational Physics **307**, 593 (2016).
[8] S. Ghosh and P. Suryanarayana, Computer Physics Communications **212**, 189 (2017).
[9] S. Ghosh and P. Suryanarayana, Computer Physics Communications **216**, 109 (2017).
[10] X. Andrade, D. Strubbe, U. De Giovannini, A. H. Larsen, M. J. T. Oliveira, J. Alberdi-Rodriguez, A. Varas,

- I. Theophilou, N. Helbig, M. J. Verstraete, L. Stella, F. Nogueira, A. Aspuru-Guzik, A. Castro, M. A. L. Marques, and A. Rubio, *Physical Chemistry Chemical Physics* **17**, 31371 (2015).
- [11] J. Enkovaara, C. Rostgaard, J. J. Mortensen, J. Chen, M. Dulak, L. Ferrighi, J. Gavnholt, C. Glinsvad, V. Haikola, H. A. Hansen, H. H. Kristoffersen, M. Kuisma, A. H. Larsen, L. Lehtovaara, M. Ljungberg, O. Lopez-Acevedo, P. G. Moses, J. Ojanen, T. Olsen, V. Petzold, N. A. Romero, J. Stausholm-Møller, M. Strange, G. A. Tritsaris, M. Vanin, M. Walter, B. Hammer, H. Häkkinen, G. K. H. Madsen, R. M. Nieminen, J. K. Nørskov, M. Puska, T. T. Rantala, J. Schiøtz, K. S. Thygesen, and K. W. Jacobsen, *Journal of Physics: Condensed Matter* **22**, 253202 (2010).
- [12] E. Tsuchida and M. Tsukada, *Physical Review B* **52**, 5573 (1995).
- [13] E. Tsuchida and M. Tsukada, *Physical Review B - Condensed Matter and Materials Physics* **54**, 7602 (1996).
- [14] J. E. Pask, B. M. Klein, C. Y. Fong, and P. A. Sterne, *Physical Review B* **59**, 12352 (1999).
- [15] J. E. Pask and P. A. Sterne, *Modelling and Simulation in Materials Science and Engineering* **13**, R71 (2005).
- [16] E. J. Bylaska, M. Holst, and J. H. Weare, *Journal of Chemical Theory and Computation* **5**, 937 (2009).
- [17] P. Suryanarayana, V. Gavini, T. Blesgen, K. Bhatlacharya, and M. Ortiz, *Journal of the Mechanics and Physics of Solids* **58**, 256 (2010).
- [18] P. Motamarri, M. Nowak, K. Leiter, J. Knap, and V. Gavini, *Journal of Computational Physics* **253**, 308 (2013).
- [19] V. Schauer and C. Linder, *Journal of Computational Physics* **250**, 644 (2013).
- [20] H. Chen, X. Dai, X. Gong, L. He, and A. Zhou, *Multiscale Modeling & Simulation* **12**, 1828 (2014).
- [21] D. Davydov, T. D. Young, and P. Steinmann, *International Journal for Numerical Methods in Engineering* **106**, 863 (2016).
- [22] B. Kanungo and V. Gavini, *Physical Review B* **95**, 035112 (2017).
- [23] B. Kanungo and V. Gavini, *Physical Review B* **100**, 115148 (2019).
- [24] P. Motamarri, S. Das, S. Rudraraju, K. Ghosh, D. Davydov, and V. Gavini, *Computer Physics Communications* **246**, 106853 (2020).
- [25] S. Das, P. Motamarri, V. Gavini, B. Turcksin, Y. W. Li, and B. Leback, in *Proceedings of the International Conference for High Performance Computing, Networking, Storage and Analysis*, Vol. 11 (ACM, New York, NY, USA, 2019) pp. 1–11.
- [26] O. Čertík, J. E. Pask, I. Fernando, R. Goswami, N. Sukumar, L. A. Collins, G. Manzini, and J. Vackář, *Computer Physics Communications* **297**, 109051 (2024).
- [27] L. Genovese, A. Neelov, S. Goedecker, T. Deutsch, S. A. Ghasemi, A. Willand, D. Caliste, O. Zilberberg, M. Rayson, A. Bergman, and R. Schneider, *The Journal of Chemical Physics* **129**, 10.1063/1.2949547 (2008).
- [28] L. Genovese, M. Ospici, T. Deutsch, J.-F. Méhaut, A. Neelov, and S. Goedecker, *The Journal of Chemical Physics* **131**, 10.1063/1.3166140 (2009).
- [29] S. Mohr, L. E. Ratcliff, P. Boulanger, L. Genovese, D. Caliste, T. Deutsch, and S. Goedecker, *The Journal of Chemical Physics* **140**, 10.1063/1.4871876 (2014).
- [30] W. Hu, L. Lin, and C. Yang, *The Journal of Chemical Physics* **143**, 10.1063/1.4931732 (2015).
- [31] P. Motamarri, V. Gavini, and T. Blesgen, *Physical Review B* **93**, 125104 (2016).
- [32] C.-C. Lin, P. Motamarri, and V. Gavini, *npj Computational Materials* **7**, 50 (2021).
- [33] C.-C. Lin and V. Gavini, *Computer Physics Communications* **282**, 108516 (2023).
- [34] D. Naveh, L. Kronik, M. L. Tiago, and J. R. Chelikowsky, *Physical Review B* **76**, 153407 (2007).
- [35] D. Naveh and L. Kronik, *Solid State Communications* **149**, 177 (2009).
- [36] B. Zhang, X. Jing, Q. Xu, S. Kumar, A. Sharma, L. Erlandson, S. J. Sahoo, E. Chow, A. J. Medford, J. E. Pask, and P. Suryanarayana, *Software Impacts* **20**, 100649 (2024).
- [37] W. Lu, E. Briggs, J. Bernholc, A. Pham, and P. Ganesh, in *APS March Meeting Abstracts*, APS Meeting Abstracts, Vol. 2021 (2021) p. S19.012.
- [38] S. Das, B. Kanungo, V. Subramanian, G. Panigrahi, P. Motamarri, D. Rogers, P. M. Zimmerman, and V. Gavini, *International Conference for High Performance Computing, Networking, Storage and Analysis*, SC 10.1145/3581784.3627037 (2023).
- [39] S. Das, P. Motamarri, V. Subramanian, D. M. Rogers, and V. Gavini, *Computer Physics Communications* **280**, 108473 (2022).
- [40] G. Panigrahi, N. Kodali, D. Panda, and P. Motamarri, *Journal of Parallel and Distributed Computing* **192**, 104925 (2024).
- [41] K. Ramakrishnan, S. Das, and P. Motamarri, arXiv:2408.00504 (2024).
- [42] R. Zhuravel, H. Huang, G. Polycarpou, S. Polydorides, P. Motamarri, L. Katrivas, D. Rotem, J. Sperling, L. A. Zotti, A. B. Kotlyar, J. C. Cuevas, V. Gavini, S. S. Skourtis, and D. Porath, *Nature Nanotechnology* **15**, 836 (2020).
- [43] V. Menon, S. Das, V. Gavini, and L. Qi, *Acta Materialia* **264**, 119515 (2024).
- [44] P. Kumar, M. M. Ludhwani, S. Das, V. Gavini, A. Kanjarla, and I. Adlakha, *International Journal of Plasticity* **165**, 103613 (2023).
- [45] M. F. Shojaei, J. Holber, S. Das, G. Teichert, T. Mueller, L. Hung, V. Gavini, and K. Garikipati, *Journal of the Mechanics and Physics of Solids* **190**, 105726 (2024).
- [46] L. Yao, S. Das, X. Liu, K. Wu, Y. Cheng, V. Gavini, and B. Xiao, *Journal of Physics D: Applied Physics* **55**, 455501 (2022).
- [47] K. Ghosh, H. Ma, V. Gavini, and G. Galli, *Physical Review Materials* **3**, 043801 (2019).
- [48] K. Ghosh, H. Ma, M. Onizhuk, V. Gavini, and G. Galli, *npj Computational Materials* **7**, 123 (2021).
- [49] B. Kanungo, P. M. Zimmerman, and V. Gavini, *Nature Communications* **10**, 4497 (2019).
- [50] P. Motamarri and V. Gavini, *Physical Review B* **97**, 165132 (2018).
- [51] A. D. Corso and A. M. Conte, *Physical Review B* **71**, 115106 (2005).
- [52] M. Methfessel, *Physical Review B* **52**, 8074 (1995).
- [53] K. W. Jacobsen, J. K. Nørskov, and M. J. Puska, *Physical Review B* **35**, 7423 (1987).
- [54] J. Kubler, K. H. Hock, J. Sticht, and A. R. Williams, *Journal of Physics F: Metal Physics* **18**, 469 (1988).
- [55] U. v. Barth and L. Hedin, *Journal of Physics C: Solid State Physics* **5**, 1629 (1972).

- [56] S. Lehtola, C. Steigemann, M. J. Oliveira, and M. A. Marques, *SoftwareX* **7**, 1 (2018).
- [57] K. Knöpfle, L. M. Sandratskii, and J. Kübler, *Physical Review B* **62**, 5564 (2000).
- [58] I. W. Bulik, G. Scalmani, M. J. Frisch, and G. E. Scuseria, *Physical Review B* **87**, 035117 (2013).
- [59] Z. Pu, H. Li, N. Zhang, H. Jiang, Y. Gao, Y. Xiao, Q. Sun, Y. Zhang, and S. Shao, *Physical Review Research* **5**, 013036 (2023).
- [60] D. R. Hamann, *Physical Review B* **88**, 085117 (2013).
- [61] R. M. Martin, *Electronic Structure* (Cambridge University Press, 2020).
- [62] N. D. Rufus and V. Gavini, *Physical Review B* **106**, 085108 (2022).
- [63] S. C. Brenner and L. R. Scott, *The Mathematical Theory of Finite Element Methods*, Texts in Applied Mathematics, Vol. 15 (Springer New York, New York, NY, 2008).
- [64] T. J. R. Hughes, *The Finite Element Method: Linear Static and Dynamic Finite Element Analysis*, Dover Civil and Mechanical Engineering (Dover Publications, 2012).
- [65] K.-J. Bathe, *Finite Element Procedures* (Prentice Hall, 2006).
- [66] P. G. Ciarlet, *The Finite Element Method for Elliptic Problems* (Society for Industrial and Applied Mathematics, 2002).
- [67] J. A. White and D. M. Bird, *Physical Review B* **50**, 4954 (1994).
- [68] D. Bylander and L. Kleinman, *Journal of Computational Physics* **136**, 599 (1997).
- [69] L. C. Balbás, J. L. Martins, and J. M. Soler, *Physical Review B* **64**, 165110 (2001).
- [70] G. Kresse and J. Furthmüller, *Computational Materials Science* **6**, 15 (1996).
- [71] G. Kresse and J. Furthmüller, *Physical Review B* **54**, 11169 (1996).
- [72] P. Giannozzi, S. Baroni, N. Bonini, M. Calandra, R. Car, C. Cavazzoni, D. Ceresoli, G. L. Chiarotti, M. Cococcioni, I. Dabo, A. D. Corso, S. de Gironcoli, S. Fabris, G. Fratesi, R. Gebauer, U. Gerstmann, C. Gougoussis, A. Kokalj, M. Lazzeri, L. Martin-Samos, N. Marzari, F. Mauri, R. Mazzarello, S. Paolini, A. Pasquarello, L. Paulatto, C. Sbraccia, S. Scandolo, G. Sclauzero, A. P. Seitsonen, A. Smogunov, P. Umari, and R. M. Wentzcovitch, *Journal of Physics: Condensed Matter* **21**, 395502 (2009).
- [73] P. Giannozzi, O. Andreussi, T. Brumme, O. Bunau, M. Buongiorno Nardelli, M. Calandra, R. Car, C. Cavazzoni, D. Ceresoli, M. Cococcioni, N. Colonna, I. Carnimeo, A. Dal Corso, S. de Gironcoli, P. Delugas, R. A. DiStasio, A. Ferretti, A. Floris, G. Fratesi, G. Fugallo, R. Gebauer, U. Gerstmann, F. Giustino, T. Gorni, J. Jia, M. Kawamura, H.-Y. Ko, A. Kokalj, E. Küçükbenli, M. Lazzeri, M. Marsili, N. Marzari, F. Mauri, N. L. Nguyen, H.-V. Nguyen, A. Otero-de-la Roza, L. Paulatto, S. Poncé, D. Rocca, R. Sabatini, B. Santra, M. Schlipf, A. P. Seitsonen, A. Smogunov, I. Timrov, T. Thonhauser, P. Umari, N. Vast, X. Wu, and S. Baroni, *Journal of Physics: Condensed Matter* **29**, 465901 (2017).
- [74] N. Kodali, K. Ramakrishnan, and P. Motamarri, *Manuscript under preparation* (2024).
- [75] D. G. Anderson, *Journal of the ACM* **12**, 547 (1965).
- [76] V. Eyert, *Journal of Computational Physics* **124**, 271 (1996).
- [77] G. P. Kerker, *Physical Review B* **23**, 3082 (1981).
- [78] R. Resta, *Physical Review B* **16**, 2717 (1977).
- [79] Y. Zhou, Y. Saad, M. L. Tiago, and J. R. Chelikowsky, *Physical Review E* **74**, 066704 (2006).
- [80] Y. Zhou, J. R. Chelikowsky, and Y. Saad, *Journal of Computational Physics* **274**, 770 (2014).
- [81] H. A. van der Vorst, *Mathematics of Computation* **39**, 559 (1982).
- [82] C. Cantwell, S. Sherwin, R. Kirby, and P. Kelly, *Computers & Fluids* **43**, 23 (2011).
- [83] G. F. Carey, E. Barragy, R. McLay, and M. Sharma, *Communications in Applied Numerical Methods* **4**, 299 (1988).
- [84] T. J. Hughes, R. M. Ferencz, and J. O. Hallquist, *Computer Methods in Applied Mechanics and Engineering* **61**, 215 (1987).
- [85] *ACM Transactions on Mathematical Software* **28**, 135 (2002).
- [86] P. Giannozzi, S. Baroni, N. Bonini, M. Calandra, R. Car, C. Cavazzoni, D. Ceresoli, G. L. Chiarotti, M. Cococcioni, I. Dabo, A. Dal Corso, S. de Gironcoli, S. Fabris, G. Fratesi, R. Gebauer, U. Gerstmann, C. Gougoussis, A. Kokalj, M. Lazzeri, L. Martin-Samos, N. Marzari, F. Mauri, R. Mazzarello, S. Paolini, A. Pasquarello, L. Paulatto, C. Sbraccia, S. Scandolo, G. Sclauzero, A. P. Seitsonen, A. Smogunov, P. Umari, and R. M. Wentzcovitch, *Journal of physics. Condensed matter : an Institute of Physics journal* **21**, 395502 (2009).
- [87] I. Carnimeo, F. Affinito, S. Baroni, O. Baseggio, L. Bellentani, R. Bertossa, P. D. Delugas, F. F. Ruffino, S. Orlandini, F. Spiga, and P. Giannozzi, *Journal of Chemical Theory and Computation* **19**, 6992 (2023).
- [88] F. F. Ruffino, L. Bellentani, G. Rossi, F. Affinito, S. Baroni, O. Baseggio, P. Delugas, P. Giannozzi, J. Kurzak, Y. Luo, O. O'Reilly, S. Orlandini, and I. Carnimeo, *Procedia Computer Science* **240**, 52 (2024).
- [89] J. P. Perdew, K. Burke, and M. Ernzerhof, *Phys. Rev. Lett.* **77**, 3865 (1996).
- [90] M. van Setten, M. Giantomassi, E. Bousquet, M. Verstraete, D. Hamann, X. Gonze, and G.-M. Rignanese, *Computer Physics Communications* **226**, 39 (2018).
- [91] P. Scherpelz, M. Govoni, I. Hamada, and G. Galli, *Journal of Chemical Theory and Computation* **12**, 3523 (2016).
- [92] H. Monkhorst and J. Pack, *Physical Review B* **13**, 5188 (1976).
- [93] G. Makov and M. C. Payne, *Physical Review B* **51**, 4014 (1995).
- [94] P. J. Linstrom and W. G. Mallard, *NIST Chemistry WebBook, NIST Standard Reference Database Number 69* (National Institute of Standards and Technology, Gaithersburg MD, 20899, 2024).
- [95] S. Ayaz Khan, P. Blaha, H. Ebert, J. Minár, and O. Šipr, *Physical Review B* **94**, 144436 (2016).
- [96] M. Blanco-Rey, J. I. Cerdá, and A. Arnau, *New Journal of Physics* **21**, 073054 (2019).
- [97] A. Jain, S. P. Ong, G. Hautier, W. Chen, W. D. Richards, S. Dacek, S. Cholia, D. Gunter, D. Skinner, G. Ceder, and K. A. Persson, *APL Materials* **1**, 10.1063/1.4812323 (2013).
- [98] J.-W. Luo, G. Bester, and A. Zunger, *Physical Review Letters* **102**, 056405 (2009).
- [99] N. E. Christensen, *Physical Review B* **30**, 5753 (1984).